

UNIVERSITY OF CALIFORNIA
SANTA CRUZ

**NOVEL PHOTOVOLTAICS: AN INTRODUCTION TO BASIC
CHARACTERIZATION**

A dissertation submitted in partial satisfaction of the
requirements for the degree of

DOCTOR OF PHILOSOPHY

in

PHYSICS

by

Jeremy D. Olson

June 2009

The Dissertation of Jeremy D. Olson
is approved:

Professor Sue Carter, Chair

Professor Glenn Alers

Professor Frank Bridges

Lisa C. Sloan
Vice Provost and Dean of Graduate Studies

Copyright © by

Jeremy D. Olson

2009

Table of Contents

| | |
|--|-------------|
| Abstract | v |
| List of Figures | vi |
| List of Tables | viii |
| Dedication | ix |
| Acknowledgments | x |
| 1 Introduction | 1 |
| 1.1 Why Solar? | 1 |
| 1.2 Materials | 3 |
| 1.2.1 Energy bands | 5 |
| 1.2.2 Differences between inorganic and organic semiconductors | 8 |
| 1.2.3 Carrier concentrations, dopants, and impurities | 12 |
| 1.2.4 Nanocrystals | 16 |
| 1.3 Modeling the photovoltaic circuit | 19 |
| 1.4 Optical properties | 24 |
| 1.4.1 Franck-Condon fluorescence | 24 |
| 1.4.2 Urbach absorption tail | 26 |
| 2 Luminescent Solar Concentrators | 28 |
| 2.1 Computer Simulation of LSC | 32 |
| 2.2 Loss Mechanisms in LSC's | 36 |
| 2.2.1 Measuring a small absorption coefficient | 40 |
| 2.3 Simulation Results | 43 |
| 2.3.1 Urbach absorption: open questions | 50 |
| 2.4 Conclusion | 53 |

| | | |
|----------|---|-----------|
| 3 | Bulk Heterojunction solar cells | 55 |
| 3.1 | Introduction | 55 |
| 3.2 | Fabrication and Treatment | 58 |
| 3.3 | Experimental | 59 |
| 3.4 | Results/Discussion | 61 |
| 3.5 | Conclusion | 68 |
| 4 | Inorganic Thin-Film | 69 |
| 4.1 | Sintered nanocrystal films | 69 |
| 4.2 | Conclusion | 79 |
| 5 | Conclusion | 80 |
| A | Optical techniques | 82 |
| A.1 | Monochromator Calibration | 82 |
| A.2 | Measuring External Quantum Efficiency | 85 |
| A.2.1 | Counting Photons | 86 |
| A.3 | Measuring Fluorescence Quantum Yield | 87 |
| B | Monte-Carlo Simulation | 90 |
| B.1 | Random Generation of a Spectrum | 90 |
| B.2 | Generating random points on a unit sphere | 91 |
| | Bibliography | 92 |

Abstract

Novel photovoltaics: an introduction to basic characterization

by

Jeremy D. Olson

Through simulation and experimental devices, we show three means to achieve solar power via very low cost techniques and find parameters important to optimize power efficiency. For the case of luminescent solar concentrators, highly photoluminescent materials with emission in the near-IR must be used. We show that LSC's should provide an affordable route to solar energy with a realistic set of material properties.

For blended CdSe nanocrystal/P3HT thin films, we have show that the morphology depends mostly upon material preparation and device processing, and that the phase separation is dominated by the nanocrystal ligand population. Controlling this morphology is expected to be challenging, and, given the limits of the exciton diffusion length and typical large-scale phase separation, this technology will be difficult to develop into a product using CdSe nanodots.

We also show that sintered CdTe nanocrystals behave like traditional inorganic Schottky diodes. We find improved optical density accompanying the grain growth that occurs with high temperature exposure to CdCl₂, providing an additional mechanism for improvement in our films and the established CdS/CdTe solar cell films. We also discuss evidence for a cadmium-rich conducting layer formed at the grain boundaries.

List of Figures

| | | |
|------|--|----|
| 1.1 | Costs and efficiencies of first, second, and third generation photovoltaics. | 3 |
| 1.2 | Semiconductor band structure. | 5 |
| 1.3 | π -bonding in a chain of carbon atoms. | 8 |
| 1.4 | Exciton splitting and resulting transport in donor-acceptor photovoltaics. | 9 |
| 1.5 | Schottky barrier formation. | 12 |
| 1.6 | A simple picture of multiple exciton generation. | 20 |
| 1.7 | Equivalent circuit for a photovoltaic device and expected J-V behavior. | 21 |
| 1.8 | Spectral symmetry for Franck-Condon fluorescence. | 25 |
| 1.9 | Illustration of the Franck-Condon principle. | 26 |
| 1.10 | Allowed optical transitions for ideal and realistic semiconductors. | 27 |
| | | |
| 2.1 | Photograph of experimental luminescent solar concentrators. | 29 |
| 2.2 | Trapping efficiency for diffuse, fluoresced light by index of refraction. | 30 |
| 2.3 | Absorption and emission spectra of a red polyfluorine. | 31 |
| 2.4 | Monte-Carlo simulation steps for LSC's. | 32 |
| 2.5 | AM1.5 Global photon flux density and silicon responsivity. | 35 |
| 2.6 | Photon loss from misaligned LSC faces. | 39 |
| 2.7 | LSC emission spectra as a function of excitation source position. | 40 |
| 2.8 | Absorption coefficients measured inside emission bandwidth. | 42 |
| 2.9 | Redshift of experimental and simulated LSC emission spectra. | 43 |
| 2.10 | Correlation between simulated and experimental LSC's. | 45 |
| 2.11 | Material performance for various G_{geo} . | 48 |
| 2.12 | Fluorescence and absorption for various materials. | 49 |
| | | |
| 3.1 | Device structure and transport mechanism for a BHJ solar cell. | 55 |
| 3.2 | Energy diagram and schematic of CdSe/P3HT blended devices. | 59 |
| 3.3 | Morphology and J-V for BHJ films with various capping ligands. | 61 |
| 3.4 | Morphology and J-V for films spun with additional ligand. | 63 |
| 3.5 | Morphology and J-V showing NC batch dependence | 64 |
| 3.6 | Photovoltaic parameters evolution during thermal anneal. | 65 |
| 3.7 | J-V after long anneal at various temperatures to show P3HT shunting. | 66 |

| | | |
|-----|---|----|
| 3.8 | Champion J-V for BHJ films. | 67 |
| 4.1 | Device structure (a) and energy diagram (b). | 70 |
| 4.2 | SEM and optical absorption for CdTe NC films before/after CdCl ₂ | 70 |
| 4.3 | J-V and EQE for CdTe Schottky diodes. | 77 |
| 4.4 | EQE for devices of varying thicknesses. | 78 |
| 4.5 | Arrhenius plot and C-V evidence for Schottky barrier. | 78 |
| A.1 | A simplified monochromator schematic | 83 |

List of Tables

| | | |
|-----|---|----|
| 2.1 | Simulated and measured LSC efficiencies. | 46 |
| 2.2 | Expected η compared with spectral overlap (λ^*). | 47 |
| 2.3 | Currents expected with and without Urbach photoluminescence. | 52 |
| 2.4 | Effects of Urbach PL at small and large G_{geo} | 53 |

Dedicated to Mila,
the best friend I've ever had.

Acknowledgments

I want to recognize the researchers in the Carter-Alers conglomerate who helped me with these projects...Glenn Gray, Lily Yang, Tong Ju, Joyce Zhou, Veronica Sholin, Alison Breeze, Chris France, Yvonne Rodriguez, Ingrid Anderson, and Josh Ford. It was a pleasure to work with all of you.

I would also like to thank Dr. Rena Zieve, my undergraduate adviser. I didn't believe I would succeed as a graduate student, but Dr. Zieve had faith in me and taught me the fundamentals of condensed matter theory and experiment. I was very lucky to have such an effective and caring mentor.

I appreciate the efforts of my committee to ensure this text was as well-written and accurate as possible, especially Dr. Bridges. Few pages went undecorated by his corrections in the first draft, and the text is much more precise thanks to his editing.

I want to thank Pete Phelan, my seventh and eighth grade science teacher. Many people enter college unsure of what path to take until they are inspired by one of their professors. Mr. Phelan inspired me in middle school.

I owe my friends and family thanks for their support, especially my parents, who taught me to value education and sent me into the world well-prepared.

More than anyone, though, I owe thanks to Dr. Sue Carter for the opportunity to do this research. Working with her has been a privilege. I only wish she were more selfish, and had insisted I remain another year or two instead of encouraging me to move on now that I'm showing signs of competence.

Chapter 1

Introduction

1.1 Why Solar?

The global demand for energy is rising every year. Although scientists have provided many alternative energy solutions, the dominant source of electricity today comes from coal and oil because they are cheap, energy dense, and available nearly everywhere. Coal and oil are, however, filthy technologies when their energy is harvested on the cheap, and our supply of coal and oil is finite. What's more, by burning coal and oil, we are extracting carbon that has been trapped in the Earth's crust for millions of years and stuffing it in one geologic instant into the atmosphere.¹ The atmospheric carbon content is, in all likelihood, the cause of global warming, and the ultimate consequences of continuing to change the atmosphere are largely unforeseeable and irreversible.

¹This doesn't actually need to be so. Clean coal technology recovers the CO₂ and pumps it back into the Earth's crust, but clean coal is not in wide use for the same reason solar isn't in wide use: it's expensive.

Solar energy offers one particularly elegant solution to growing energy demands. Most renewable energies ultimately get their energy from the sun; actually, it's hard to imagine a source of energy, renewable or otherwise, we could use that do not originate from the sun.² Coal is organic material created by photosynthesis and stored underground for millions of years. Oil is also organic material stored for millions of years—essentially the result photosynthesis. So as these resources become depleted, it seems natural that we would turn to direct harvesting of solar energy. Sunlight is plentiful, free, and contains a breathtaking amount of energy. For example, California used 270 Terra-watt hours in 2007 [98]. According to a California Energy Commission report, if commercial buildings were paneled with moderate efficiency (10%) solar panels, over 100 TWh would be generated annually. If solar panels were placed everywhere practical, we would generate 100 TWh *every day*. [79]

The trouble with solar energy is the cost. Silicon photovoltaics cost around three dollars per watt, and this price cannot be reduced by simply scaling up production; the bulk of silicon photovoltaics are made from refined silicon scrap [76]. To find a more cost effective solution to our energy problem, here we research luminescent solar concentrators and thin-film solar cells based on polymers and inorganic nanocrystals.

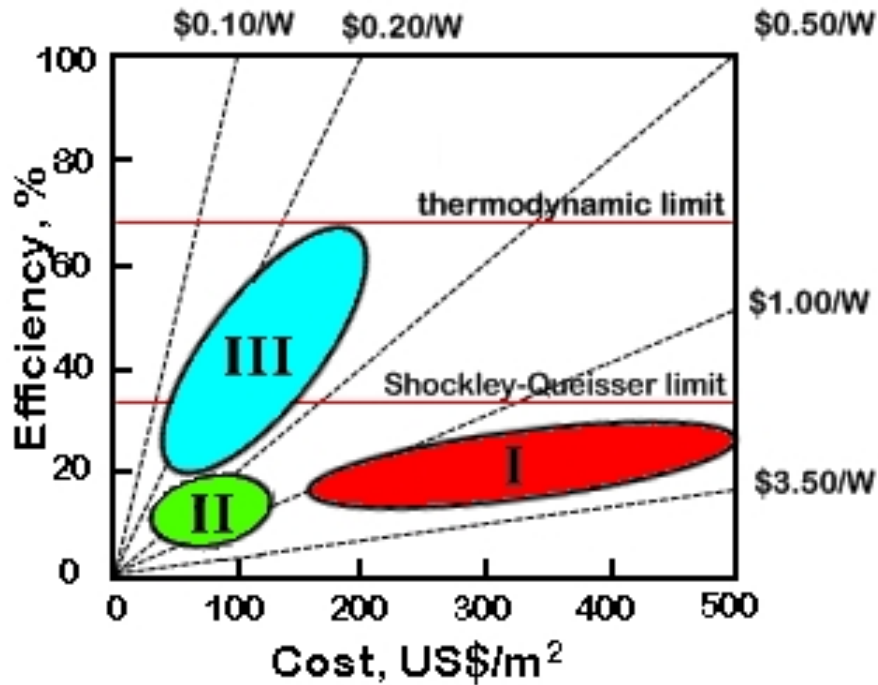


Figure 1.1: Possible cost and efficiency distributions of first, second, and third generation solar cells.

1.2 Materials

Photovoltaics (PV) are often categorized into first, second, and third generation by their materials. Figure 1.1 roughly depicts projected cost and efficiency possibilities for first, second, and third generation solar cells. First generation solar cells are based on crystalline silicon, and currently dominate the PV market. Second generation solar cells are usually defined as thin-film cells, including amorphous silicon (a-Si), cadmium telluride (CdTe), and cadmium indium gallium selenide (CIGS). Of those three, a-Si is by far the dominant technology in production. CIGS solar cells have

²Tidal energy and nuclear energy are two examples of energy sources that don't originate from our sun.

the highest laboratory efficiencies [66], but are not commercially available at the time of writing. First Solar, a CdTe solar panel manufacturer, has claimed to have the cheapest production cost per watt as of 2009 [81].

There are a few definitions of what qualifies as a third generation solar cell. Figure 1.1 suggests that the proper definition of a third-generation photovoltaic technology should be, “a low cost, high efficiency technology capable of surpassing the Shockley-Queisser limit.” (The Shockley-Queisser limit will be described below in 1.3.) However, frequently this definition is relaxed to include any extremely low-cost solar technology even if the Shockley-Queisser limit cannot be surpassed. In effect, the classification of third or second generation solar cells becomes largely material dependent, so dye-sensitized solar cells, polymer-based solar cells, or nanocrystal solar cells are usually referred to as third generation. At the time of writing, the record efficiency for a third generation solar cell stands at 11%, achieved by Chiba *et al.* [16], but progress is being made quickly using polymers. The Alan Heeger group at UC Santa Barbara has produced a 6.5% efficient device using thin-films of polymers. [43]

In this research, we study third-generation solar cells using the more loose, material-based definition. So before discussing the details of photovoltaic devices, we’ll discuss the properties of the materials studied: nanocrystals, polymers, and thin inorganic films.

1.2.1 Energy bands

Semiconductors, metals, and insulators are not fundamentally different from each other; the size of the bandgap (E_g), carrier concentration (n_{e^-} or n_{h^+}) and position of the fermi level (E_f) will determine which category a given material fits into, and all three types of materials are useful in photovoltaics, either as photoactive absorbers, contacts, or tunneling barriers. Since we are mostly interested in the photoactive absorber, we'll consider the properties of semiconductors and how a polymer can act as a semiconductor.

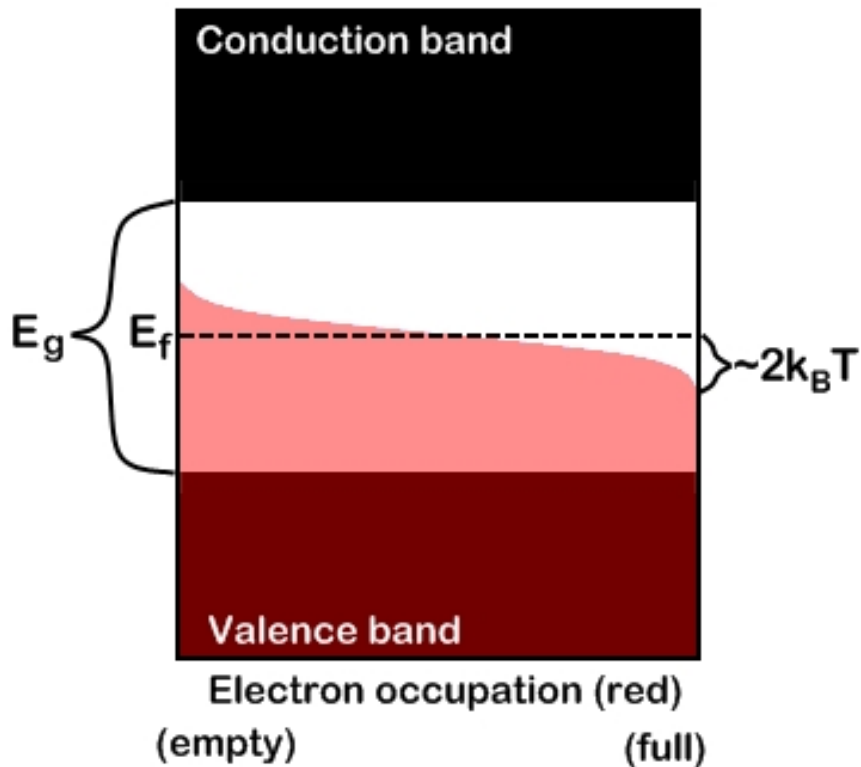


Figure 1.2: Standard energy band structure for an intrinsic semiconductor. Occupied states are shaded red.

The position of the fermi energy in the bandgap determines the semiconductor type; n-type semiconductors have more free electrons than holes, and vice versa for p-type semiconductors. At absolute zero temperature, all electrons will seek the lowest available energy state, and the energy states below E_f will be fully occupied while those above are completely empty. At finite temperature, the occupation of states will obey the Fermi-Dirac distribution

$$f(E) = \frac{1}{e^{(E-E_f)/k_B T} + 1}$$

The actual populations of free carriers will be the product of the electronic density of states and the Fermi distribution. ($g(E) \cdot f(E)$) Energy levels in semiconductors are reported relative to vacuum...typical E_f are around 5eV lower than vacuum, and E_g of interest are around usually between one and two eV. The large band of energies above E_f is known as the conduction band, and those below are known as the valence band. The mechanism for their formation is a consequence of the symmetry caused by having an extended crystalline structure as described in [86]. Any deviation from this perfect crystal will have some consequence in the energy-band structure. Grain boundaries, for example, introduce local barriers in the energy band. [14] It is no coincidence that monocrystalline solar cells have the best electrical transport! Second and third generation photovoltaics are primarily concerned with reducing the cost of production, and the crystallinity of the materials used is inferior to refined silicon.

Semiconducting polymers have a similar energy structure and a similar set of parameters. A polymer is, essentially, a one-dimensional crystal of carbon atoms.

We'll consider a simple chain of carbon atoms. (See figure 1.3.) Each carbon atom has four unbound electrons—two in the p-orbitals and two in s-orbitals.³ Two of these electrons will bond with adjacent carbon atoms in linear σ -bonds, and another will σ -bond will form with a hydrogen ion not pictured. The remaining unpaired electron is in a p-orbital, extending perpendicular to the polymer backbone.

These p-orbital electrons will form π -bonds. Two electrons are needed to form a π -bond, but only one electron is available per carbon atom, so the carbon chain will be alternately singly and doubly bonded. The alternating bonds form a π energy band that extends the full length of the polymer chain, often thousands of repeat units, or hundreds of nanometers. The extended π -bonding gives the electrons an extended region to delocalize and provides some torsional stability to the polymer.

The p-orbitals contain a spin-up state and a spin-down state. When the π -band forms, the number of states is conserved. A low energy π -band from bonding molecular orbitals, and a higher energy π^* -band forms from the anti-bonding orbitals. These two bands are more frequently called the HOMO (highest occupied molecular orbital) and LUMO (lowest unoccupied molecular orbital).

A polymer with this alternate single/double bonding is known as a conjugated polymer, or sometimes co-polymer. By adding different sidegroups, repeat units, or adsorbed ions, the energy gap, carrier concentration, and fermi energy can all be adjusted such that the material can act as a metal, insulator, or semiconductor [37].

Polyacetylene is the simplest of these polymers, but the structure of the repeat units

³Actually, the electrons for carbon atoms wind up forming s-p hybrid orbitals, but that level of detail is unnecessary for this discussion.

can become very complex. Fullerenes are also used in organic photovoltaics as they contain this alternate singly/doubly bound carbon ion pattern.

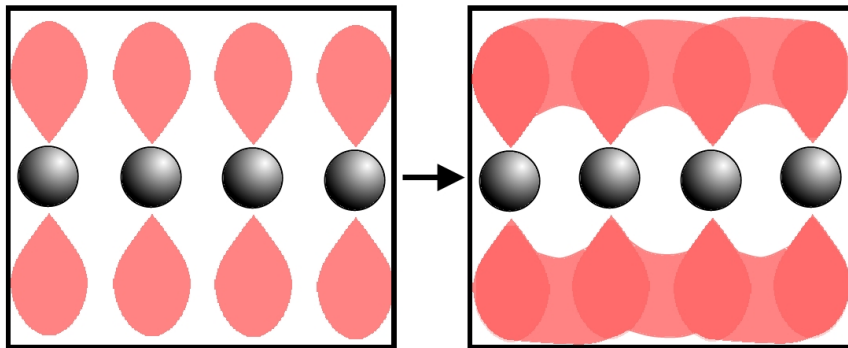


Figure 1.3: π -bonding in a chain of carbon atoms. The remaining three orbital electrons are used in σ -bonds to adjacent carbon atoms and one additional atom (not shown). This is the chemical structure of polyacetylene, the simplest conjugated polymer.

1.2.2 Differences between inorganic and organic semiconductors

Inorganic and organic semiconductors have different behaviors not because the physics are dramatically different, but because the associated parameters are different. We'll consider first the exciton binding energy. When a photon is absorbed, it excites an electron into the conduction band/LUMO and leaves a hole behind in the valence band/HOMO. Since these particles are oppositely charged, they are attracted to each other, so some energy is required to physically separate the two. This energy is known as the exciton binding energy. For inorganic semiconductors, the polarizability is relatively large, so the electron binding energy is quite small—around 24meV for CdTe [72]. Since this is less than the available thermal energy, the exciton becomes unbound as soon as the photon is absorbed, and free carriers result from photon absorption.

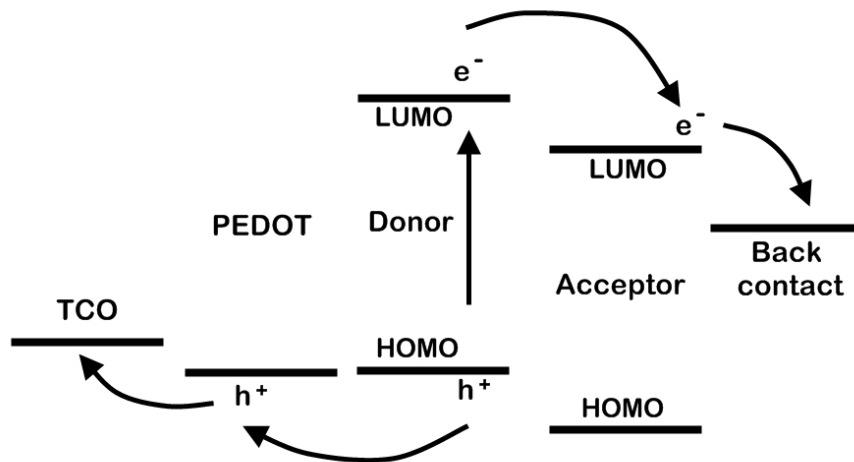


Figure 1.4: Exciton splitting and resulting transport in polymer-based photovoltaics. Poly(3,4-ethylenedioxythiophene) poly(styrenesulfonate) (PEDOT) is frequently used to inhibit electron-hole recombination in the transparent conducting oxide (TCO) layer.

In contrast, polymers have a much higher exciton binding energy of 200meV, so when a photon is absorbed, the exciton remains bound. It is for this reason that polymer-based photovoltaics always contain more than one semiconducting material. Examine figure 1.4. Ideally, one material's LUMO and HOMO levels should be closer to vacuum than the other's. With this electronic structure, it becomes favorable for the exciton to split, as the electron can relax into the low LUMO.⁴ The labels 'donor' and 'acceptor' depend upon which phase donated or accepted the electron; the material with the energy levels closest to vacuum should be the donor. The structure of these devices will be discussed in greater detail in 3.1.

⁴Typically these materials are chosen with similar E_g so that the HOMO of the donor will also be closer to vacuum than the acceptor's HOMO. So it is equally valid to argue that the exciton splits so the hole can relax into the donor's HOMO. The preferred picture depends upon which phase absorbed the photon.

There are two dominant mechanisms for exciton diffusion: Förster and Dexter energy transfer. Förster energy transfer is caused by the dipole-dipole interaction, and therefore depends upon R^{-6} , where R is the exciton hopping distance. Dexter energy transfer results from tunneling, and therefore depends upon e^{-R} . These mechanisms occur on timescales similar to the exciton lifetime, so the exciton diffusion length is only a few hopping distances—typically 5–10nm.

Mobilities for polymers are much smaller than for inorganic materials. This is partially due to material disorder, partially due to crystal anisotropy, and partially due to the polymer’s flexibility. For example, the hole mobility (μ_h) is given by

$$\mu_h = \frac{q \cdot \tau_h}{m_h^*}$$

m_h^* is the hole’s effective mass, and τ_h is the average scattering time for holes.

[30]⁵

First, we’ll compare factors that affect τ_h . For semiconductors, variations in the crystal structure will be crystal defects and grain boundaries, with grain boundaries acting as much larger energetic barriers than defects given small grains. [14] The typical monocrystalline domain sizes for CdTe are only around 50nm [11], but grain sizes can be grown to be the full thickness of the CdTe film or a significant fraction thereof. Since the crystal has symmetry along three axis, there will be little axial dependence to the transport, and τ_h will mostly depend upon grain size.

Polymers have much shorter scattering times (τ_h). Poly 3-hexylthiophene (P3HT) is one conjugated polymer in widespread use. Over short distances, the rigidity

⁵This discussion is limited to holes, but the electron transport discussion is exactly the same.

from the π -bonding and the planarity of the monomer's structure allow the polymer to crystallize, providing good transport. Over long distances, however, the polymers are disordered, so the P3HT crystallite size tends to be only around 10nm [80, 101]. Additionally, conjugated polymers will have a large axial mobility dependence [80]. It is much easier for carriers to travel along a chain than it is to hop from one chain to another. P3HT tends to align perpendicular to the desired transport direction, so carriers must hop from chain to chain in order to cross the thickness of the film, making τ_h much smaller than in crystalline semiconductors.

The polymer's flexibility is typically cited as the main reason for the large m_h^* typically measured in polymers. Rigid inorganic structures have chemical bonds in each axial direction, while even 'crystalline' polymers have no inter-chain bonds. When a carrier is excited, the lattice will distort because of unscreened coulomb interactions. These lattice distortions and their accompanying charge carriers are known as polarons. The charge carrier must drag its lattice distortion along with it as it moves, so the effective mass of the charge becomes large, and therefore the mobilities are low. Charges in crystalline materials also form polarons, but their effect is assumed to be smaller due to the inherent rigidity of the inorganic lattice.

In P3HT, the hole mobilities have been measured around $3.8 \cdot 10^{-4} \text{cm}^2 \text{V}^{-1} \text{s}^{-1}$. [5] Measured electron mobilities are more challenging to measure since P3HT is p-type, but most researchers agree that the electron mobility is smaller than the hole mobility. These low mobilities mandate that polymer photovoltaics be quite thin so charge carriers can be extracted quickly—a few hundred nanometers thick at most.

1.2.3 Carrier concentrations, dopants, and impurities

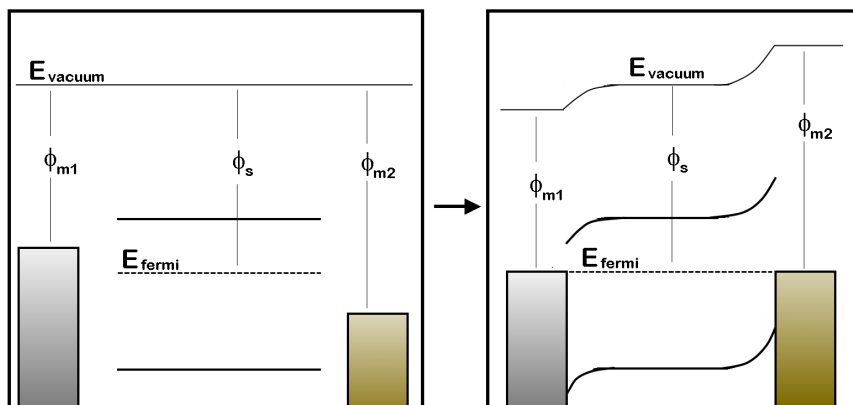


Figure 1.5: Schottky barrier formation. When semiconductors and metals contact, energy bands bend to equilibrate the fermi energy.

This discussion will be limited to the cases of inorganic and organic thin-films.⁶

Semiconductors are defined as n-type, p-type, or intrinsic. The ‘type’ of the semiconductor is determined merely by isolated Fermi level; a n-type material has an E_f above $\frac{E_g}{2}$, and E_f for a p-type material sits below $\frac{E_g}{2}$.⁷ Look at figure 1.5. Because the semiconductor work function ϕ_s sits above $\frac{E_g}{2}$, the material is n-type. In this figure, two metals are shown contacting a semiconductor. The metal on the left, m1, has a smaller work function than the metal on the right, m2 ($\phi_{m1} < \phi_{m2}$). When the metals contact the semiconductor, their fermi energies will equilibrate through charge transfer, and the energy bands will bend because of the resulting electric field. The direction of

⁶It almost certainly isn’t valid to discuss charge carrier density for an individual nanocrystal, even in the context of a fermi-level that doesn’t sit in the center of the band-gap. For the idea of carrier concentrations to make any sense, the addition of a single electron shouldn’t perturb E_f , and that is simply not the case for a single nanocrystal. Films of quantum-confined nanocrystals may be dopable, but the characterization of these films is so dependent upon processing (i.e. ligand length, size, stoichiometry, etc) that it will likely be some time before any inter-laboratory experimental repeatability will be reached.

⁷‘Above’ and ‘below’ here mean closer to and farther from vacuum, respectively.

band-bending has little to do with the type of the semiconductor; it results merely from the relative positions of the material work functions.

For thick semiconductors, these two contacts will have different behaviors. Consider a hole traveling in a n-type semiconductor—a minority carrier. Eventually, given enough distance to travel, the hole will encounter an electron and recombine. Because the hole is just as likely to encounter an electron in one undepleted region as another, the result is an exponential drop in minority carrier concentration with distance, with a characteristic length called the minority carrier diffusion length. This length for CdTe is hundreds of nanometers [90]; this is much thinner than even thin-film photovoltaics, which are microns thick. So there is essentially no current that can be carried by holes in a n-type semiconductor if the thickness is much thicker than the diffusion length, and the same is true for electrons in a p-type semiconductor.

Therefore the only carriers we're concerned in most situations are majority carriers. Examine again figure 1.5. The right contact will impede transport until a voltage is applied larger than the band bending, but the left contact will not impede charge transport for small fields. For this reason the right contact in figure 1.5 is called a rectifying contact, and the left contact is called an ohmic contact.

However, this distinction becomes much less important for films of material thinner than the minority carrier diffusion length. [60] For thin films, the distinction between rectifying and ohmic contacts are specific to a charge carrier. As stated above, the right contact in figure 1.5 is rectifying for an electron, and the left contact is ohmic. For a hole, the left contact is rectifying and the right contact is ohmic. Because the

material is thin enough to allow both charge carriers to participate in the current, the sign of the majority carrier becomes much less important.

Because the band-bending is only dependent upon relative positions of work-functions, and current can be carried by any carrier for thin films, the same band structure as a 'p-n junction' solar cell can be formed from only p-type or n-type material as long as those materials have different work-functions. Similarly, a donor-acceptor bulk-heterojunction may be formed using polymers even if both materials have the same type of excess carriers, as long as one material's LUMO/HOMO levels lie above the other's LUMO/HOMO. The photoaction can all be explained by electrons seeking easy paths to lower energy levels.

Good device engineering *will* include using n-type materials to transport electrons and p-type materials to transport holes to minimize recombination. Even with thicknesses smaller than the diffusion length, some minority carrier recombination is expected. So the message is not that the sign of the majority carriers is unimportant, but that the relative positions of the work functions are much more important. Having control over the position of the fermi level and, consequently, the majority carrier concentration is highly desirable. This is achieved by doping.

To dope a semiconductor, one introduces a small population of an ion similar to one of the semiconductor's constituent ions. For silicon, a group IV element, one typically chooses ions from groups III or V, although other materials can be used as dopants. If those ions can be incorporated into the silicon lattice, they will perturb the energy structure only slightly and provide either an additional electron (group V) or

additional hole (group III).

For the case of CdTe, doping is more complicated...tellurium is a group VI element, so group VII elements would serve as an n-dopant and group V elements would act as p-dopants *if and only if* the dopant becomes incorporated into a tellurium site. This is a big if, and we have very little control over what structure is energetically favorable for the lattice. Since processing of chalcogenide films is done at relatively high temperatures, ions will be mobile enough to diffuse through the film, including ions in the substrate. Dopants may diffuse *en masse* to grain-boundaries, in which case knowing the precise concentration of various elements in the film merely sets an upper bound on the carrier concentration. Intrinsic crystal defects, such as interstitial ions, vacant lattice sites, and cations on anion sites or *vice versa* can all act as dopants, and the effect of multiple dopants is a complicated and rich subject. [95]

In other words, it is best to measure carrier concentration and sign as directly as possible using capacitance-voltage profiling, Hall effect, or Seebeck coefficient, rather than try to predict the charge carrier concentration based upon the ionic makeup of your material unless a method of stoichiometry can be used with localization similar to the material monocrystallite size.

Polymers are a bit different. At the time of polymerization, energy levels in polymers can be shifted significantly by changing the chemical makeup of the polymer—by adding sidegroups and such. However, the chemical makeup of the polymer won't change under typical processing conditions once polymerization is complete. Polymers require relatively low temperature processing, so ions from the substrate will not dif-

fuse into and become chemically bound to the polymer. But the charge carrier density can still be manipulated. Impurities from the atmosphere, such as oxygen, or solvents can incorporate themselves into polymers, providing new energy levels/charge carriers.⁸ For alkylthiophenes (like P3HT), molecular oxygen will become absorbed into the center of the thiophene ring and take one polymer electron with it. Although this degrades transport, it also increases carrier concentration and improves conductivity [1]. Charge carrier density can still be measured using capacitance-voltage profiling [102], and HOMO/LUMO levels can be probed using cyclic voltammetry or U-V photoelectron spectroscopy.

Polymer solar cells degrade when exposed to atmosphere. Several mechanisms for this degradation exist [68]. The effects of atmospheric molecules incorporated into polymer films is varied, but, typically, a polymeric photovoltaic device is better off without any impurities, even if additional charge carriers would be desirable for some reason.

1.2.4 Nanocrystals

Nanocrystals combine some properties from organics, some from inorganics, and have some unique properties as well. There are many types of nanocrystals, from TiO₂ crystals with 100nm radii to highly structured chalcogenide crystals to nanoscale-pools of evaporated metal. For this discussion, we'll limit ourselves to solution-grown

⁸Since these materials are often introduced during processing, it might be better put that it's difficult *not* to manipulate charge carrier density.

nanocrystals using the method outlined by Gur *et al.* [33]⁹ We used both nanorods and nanodots for our research, but found no significant difference in their behavior, so we'll make no distinction between the two.

When nanocrystals are synthesized, they are often capped with organic ligands.¹⁰ These ligands serve three purposes. First, the ligands stop the nanocrystal growth. Second, the ligands make the nanocrystals soluble. And, third, the ligands take up trap states. The first two points shouldn't require explanation, and the explanation for the third is simple. For these crystals, each lattice point has four covalent bonds. Surface ions only have three covalent bonds; the fourth bond is left dangling.¹¹ Without the rest of the lattice, it's no simple matter to determine precisely where that unbound electron (and the missing electron that should be paired with it) would lie energetically. However, it's not unreasonable to assume that a covalently bound electron is going to be more similar to our crystal structure than an unbound electron, and, in any case, the ligand is required for the first two reasons.

The typical ligand of choice for cadmium-based nanocrystals is tri-octylphosphine oxide, or TOPO. This ligand is quite long, and so it is typically exchanged for another ligand, with the possibility of an intermediate ligand, typically pyridine [33]. Those who have studied the efficiency of ligand exchange via NMR report exchange efficiencies of at most 90%. [3, 13] Additional refluxing does not result in additional ligand exchange.

⁹See the online supplementary material in [33] for synthesis details.

¹⁰Nanocrystals can also be capped with another material. These are called 'core-shell' nanocrystals. All nanocrystals we used for these studies were ligand capped.

¹¹This not just true for nanocrystals, but all chalcogenide surfaces, of course. Nanocrystals just have a larger surface to volume ratio.

What's more, as a batch of nanocrystals undergoes additional ligand exchanges, the ligands exchange more slowly and with less efficiency. [13] Although we have no direct measurement of our ligand exchange efficiencies, it bears keeping in mind that these exchanges are not 100% efficient as this process is often overlooked.

Another surprising quirk of nanocrystals is their stoichiometry isn't perfect. Although the core of the nanocrystal is effective at rejecting defects, and therefore close to stoichiometric perfection, the surface of the nanocrystal comes with no such guarantee. In fact, TOPO bonds selectively with cadmium, so, if TOPO were the only ligand used, the surface would be only cadmium. To counteract this, tri-octylphosphine (TOP), which bonds with selenium/tellurium is used, but studies of nanocrystal surface stoichiometry show that, even using TOP, the nanocrystals tend to have Cd:Se ratios of about 5:4 [39, 87]. This is the total stoichiometry; the surface stoichiometry is still very cadmium rich.

The size of nanocrystals makes them similar, in ways, to organic semiconductors. For films of unsintered nanocrystals, electron mobilities are similar to organic electron mobilities, and transport is done by hopping from nanocrystal to nanocrystal in the same way that carriers must hop from chain to chain in organic semiconductors. [31] But these transport properties depend dramatically on processing. [31, 70] The exciton binding energy is low enough to expect free carriers [29], and disagreement abounds as to whether the photovoltaic behavior is more akin to a donor-acceptor device [33] or an inorganic device [53].

Because of their small size, nanocrystals have interesting and unique optical

properties. As the nanocrystal becomes smaller, the energy-levels spread out, and the effective band-gap becomes larger. This phenomenon is so well established that the optical absorption is used to measure the size of nanocrystals.

A much more interesting and mysterious phenomenon is multiple exciton generation. When a ‘normal’ semiconductor absorbs a photon, any energy in excess of the bandgap is lost. An electron excited high above the bandgap will rapidly settle to the bottom of the conduction band by coupling to phonons. However, in nanocrystals the phonon spectrum is much more discrete, so cooling by exciting phonons is a much slower process, and it becomes energetically favorable for the electron to promote additional electrons across the bandgap in order to cool. [25] This phenomenon, known as multiple exciton generation (MEG), generally becomes much more efficient for photons with energies of $3E_g$ or greater, but the details aren’t widely agreed upon beyond the fact that additional charge carriers become excited. MEG has been observed by measuring fluorescence from colloidal nanocrystals, and promising evidence that this can actually result in enhanced photocurrents exists [53], but so far no photovoltaic device has conclusively shown this photocurrent enhancement.

1.3 Modeling the photovoltaic circuit

It is useful to consider the photovoltaic device as a simple circuit as pictured in figure 1.7(a). Although a more complicated circuit can be used to more closely model the current-voltage (J-V) characteristics of solar cells, here we are only concerned with

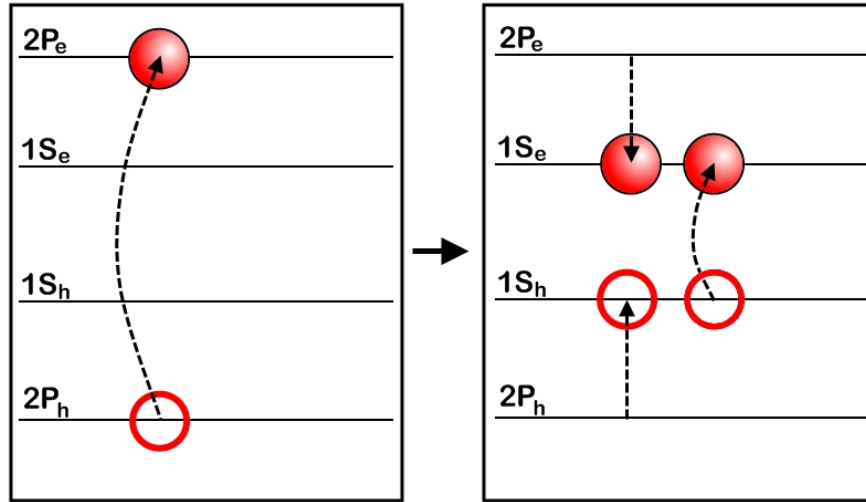


Figure 1.6: A simple picture of MEG. A photon with energy of $3E_g$ is absorbed. As the electron settles into the valence band, another electron is promoted from the conduction band. Energy levels are labeled as S and P as nanocrystals energy levels are analogous to molecular orbitals. Adapted from the description of MEG by Ellingson *et. al.* [25] The energy gap between $1S_h$ and $1S_e$ is the effective E_g .

gaining a qualitative understanding of how to interpret J-V curves in order to identify and correct flaws in photovoltaic films.¹² We'll consider each component in turn.

Important parameters for photovoltaic performance are contained in figure 1.7(b). The open-circuit voltage (V_{oc}) and short-circuit current (J_{sc}) are just what their names advertise: the voltage and current under open and short circuit conditions, respectively. These are typically measured under a simulated solar spectrum. The AM1.5G (global) and AM1.5D (direct) standards are most the commonly used.¹³ The intensity of AM1.5G is $1kWm^{-2}$, or $100mWcm^{-2}$. The AM1.5G spectrum is the expected spectrum after sunlight has passed through 1.5 atmosphere thicknesses of air, so

¹²Current density (J) is preferred over current (I) as current is expected to scale with illuminated area. Thus, current density J is not equivalent to the current density carried by the contacts, but rather current density flowing through the thickness of the photovoltaic film.

¹³Solar simulation and spectral correction is covered thoroughly in [15].

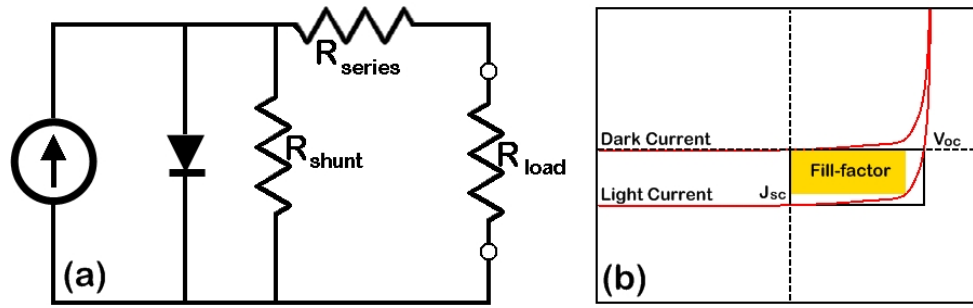


Figure 1.7: A simple equivalent circuit for a photovoltaic device (a) and the resultant J-V characteristics. The current source only provides current under illumination. Power is collected at R_{load} .

intensities at noon are actually higher in many places than AM1.5G. Subtracting the spectrum of diffuse light will from AM1.5G will result in AM1.5D, the direct spectrum. AM1.5D is used for traditional solar concentrators, which cannot harvest diffuse light.

The remaining photovoltaic parameter is the fill-factor (FF). This is usually given as a percent, and represents the “squareness” of the J-V curve. With the V_{oc} , J_{sc} , and FF parameters, one can quickly calculate the power-efficiency η of the device as

$$\eta = \frac{V_{oc} \cdot J_{sc} \cdot FF}{I_o}$$

I_o is the incident light intensity. Using AM1.5G as the illumination source is quite convenient. For good laboratory scale devices, J_{sc} will be measured in $mAc m^{-2}$, and V_{oc} in volts, so the product $J_{sc} \cdot V_{oc} \cdot FF$ yields a power in $mWcm^{-2}$. Since the light intensity happens to be $100mWcm^{-2}$, the product also is the percent efficiency.¹⁴

We’ll consider first the diode. The diode will follow a modified Shockley equation

¹⁴ FF should be expressed as a fraction in this instance, obviously.

$$J = J_o(e^{V/nk_B T} - 1)$$

J_o is the reverse saturation current, and has both an exponential and squared temperature dependence. n is known as the diode ideality factor. One might expect to be able to extract relevant physical parameters from J-V characteristics; the Shockley equation is a good example of one instance in which this is possible, although this is the exception rather than the rule at room temperature.¹⁵ At a mild forward bias, in the dark, a fit to $\ln J$ against V will yield $\frac{1}{nk_B T}$. This fit on dark currents should span forward bias for $k_B T < V < V_{oc}$. In this region, current should primarily be flowing through the diode.¹⁶ If the current is primarily flowing through R_{shunt} , the $\ln J$ will not be linear in this region and the fit will be poor.

For perfect thermionic emission, n will be one for a Schottky barrier and two for a p-n junction, although slight deviation from this on the order of 10% does not indicate significant deviation from the thermionic emission model. [86] However, higher ideality factors indicate that something is wrong with our model. Frequently, the problem is an interfacial layer, which results in a voltage-dependent barrier height.

In general, however, fitting to the room-temperature J-V curves won't yield any more physical insight than merely examining the J-V curves will [96]. Let's re-examine figure 1.7(a). Our goal is to force as much current through the load resistor as

¹⁵The barrier height mobility are difficult to measure precisely without measuring J-V over a range of temperatures.

¹⁶The driving source for this current is actually R_{load} . Measuring parameters on photovoltaic cells requires replacement of R_{load} with a voltage source.

possible. At short-circuit, the same voltage drop will be across R_{shunt} and R_{series} , since $R_{load} = 0$. Current through R_{series} , which will be equal to our J_{sc} , will be reduced from the current generated at the current source by the relation

$$J_{sc} = \frac{J_{source} \cdot R_{shunt}}{R_{series} + R_{shunt}}$$

To harvest as much current as possible, $R_{shunt} \gg R_{series}$. If this isn't true, a large number of collected photons will be lost as the current flows through R_{shunt} at short-circuit. V_{oc} and FF will also be reduced, as the primary leaking mechanism will become R_{shunt} instead of the diode, and less power will be delivered to R_{load} .¹⁷ By fitting to J-V curves, we can make estimates of R_{shunt} and R_{series} . R_{shunt} should be well described by a fit to the light current around $V = 0$, or at small reverse bias. Nearly all of the current in these configurations should be flowing through R_{shunt} . R_{series} can be measured by finding the J-V slope at forward bias provided the J-V curve shows good diode behavior.

Good values for R_{shunt} and R_{series} should be around the same order as resistances calculated using the low-field resistivity for the semiconductor and contacting materials, respectively. Our devices typically have a R_{shunt} of some mega-ohms in the dark. Too large of R_{series} values indicate resistivity at one of the two electrical-semiconductor interfaces; this will surface first as a drop in J_{sc} . If the film contains current-leaking pathways, such as pinholes, R_{shunt} will be reduced, which will result in a reduced V_{oc} . In both of these cases the fill-factor will be reduced. This is covered in great detail by Klaus. [64]

¹⁷Many laboratory devices lose more current to R_{shunt} than to the diode.

The easiest of the components to understand is the current source. If we assume each photon with energy greater than E_g excites one electron into the conduction band, we can measure the current for our device and deduce how many photons were collected. By counting the photons available in the AM1.5G spectrum for an E_g around 1.5eV, we can expect a current density of at most 30 mAcm^{-2} or so. This limit on current is known as the Shockley-Queisser limit [77]. Poor optical absorption or high rates of recombination will result in reduced J_{sc} .

The recombination rates are often spectrally dependent. For example, photons absorbed outside the depletion region will usually recombine, and the absorption length is obviously different for different wavelengths. Absorption limited devices will only absorb a small fraction of the incident light. In this case, the spectral dependence of J_{sc} should just match the absorption profile. The spectral response for a solar cell is the external quantum efficiency (EQE). It's measurement and some interpretation is given in section A.2, and in great detail by Chasteen [15].

1.4 Optical properties

1.4.1 Franck-Condon fluorescence

Some materials exhibit extraordinary symmetry between their absorption and fluorescence spectra. The reason behind this symmetry is, of course, very elegant and simple physics. This symmetry occurs when fluorescence is very fast relative to molecular vibrations, such that ions do not move during fluorescence.

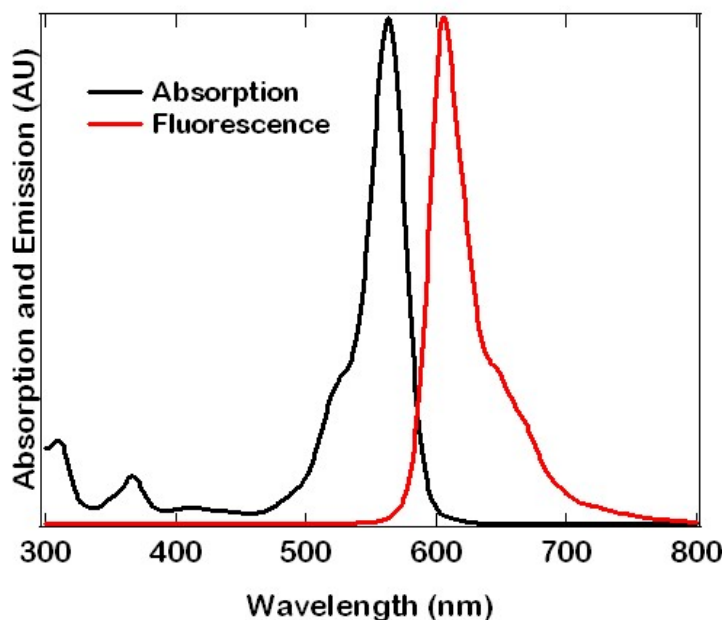


Figure 1.8: Rhodamine B gives a striking example of fluorescence symmetry from the Franck-Condon principle.

Consider figure 1.9. Two harmonic oscillator potentials, S and S' , with corresponding wavefunctions ψ_n and ψ'_n , are held at some fixed distance d from one-another.¹⁸ An electron sits in state ψ_0 of potential S . When a photon excites this electron, the electron will transition from potential S to potential S' into whichever state it has the most overlap with. (In this case, the, ψ_0 and ψ'_2 have the greatest overlap.) Once in S' , the electron will quickly settle to state ψ'_0 before fluorescing. It will now be most likely to transition $\psi'_0 \rightarrow \psi_2$. By symmetry, those wavefunctions will have the most overlap.

However, there is no corresponding symmetry between the high energy absorption and the fluorescence.¹⁹ Photons absorbed at higher energies will excite photons into

¹⁸These potentials are labeled S because they are singlet potentials. Triplet potentials are also present, but they do not exhibit Franck-Condon, as the transition from a triplet state to a singlet state is forbidden, and thus takes longer than the nuclear motion.

¹⁹Examining figure 1.8, the region we're discussing here is between 300nm and 500nm in wavelength.

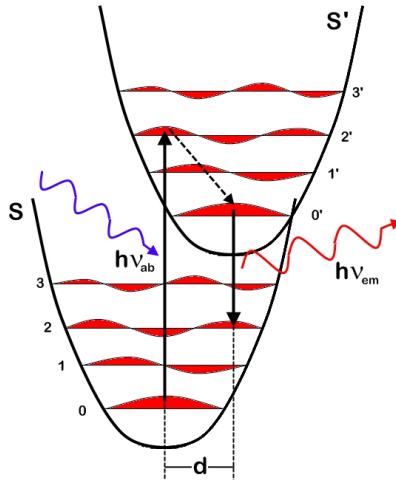


Figure 1.9: For an energy transition $\psi_0 \rightarrow \psi'_2$, a transition $\psi'_0 \rightarrow \psi_2$ will be favored.

a higher energy singlet potential, say S'' , which will quickly decay into the S' potential and fluoresce as before.

1.4.2 Urbach absorption tail

Optical absorption spectra have long tails that fall off exponentially with long wavelengths. This phenomenon is known as Urbach's rule. The absorption spectrum tail will be described by

$$\alpha(\lambda) \propto e^{-\sigma \cdot \lambda}$$

There are several [20,40] possibilities for the mechanism of this tiny absorption. We'll consider the density of states inside the bandgap as the source [40], not because that is irrefutably the source of this absorption, but merely because other properties of photovoltaic materials are also related to states inside the bandgap, so this is an instructive way to think about them.

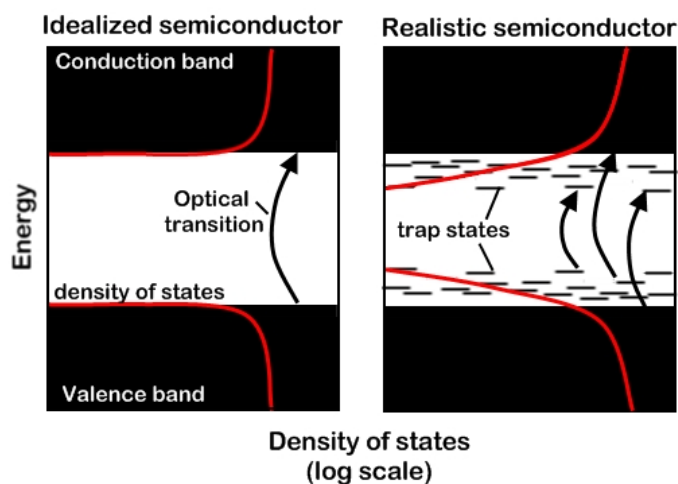


Figure 1.10: Realistic semiconducting materials have energy bands with soft edges, so sub-band transitions are possible. The density of electronic states is shown in red, and optical transitions are shown in black.

The simple energy-band structure for semiconducting materials does not tell the entire story for polymers or inorganics. Broad energy bands largely define the allowed transitions, but small numbers of ‘trap’ states exist within the band gap. This allows optical transitions smaller than the band-gap. (See figure 1.10.)

Rigorous analysis would demand that the absorption coefficient (α) falls exponentially in energy, not wavelength, but this approximation will be close enough for our purposes, since the absorption coefficient will become exponentially small as the un-even steps in energy become significant.

Chapter 2

Luminescent Solar Concentrators

Normal solar concentrators typically employ mirrors to focus light onto a highly efficient silicon solar cell. The idea is to save money; mirrors are much cheaper than silicon, so light can be collected over a large area and concentrated onto an efficient cell. There are some problems with this.

- Using mirrors necessitates the use of tracking motors to continually realign the focal point as the sun traverses the sky, and these are expensive.
- Optical condensers cannot harvest diffuse light, which makes up a significant fraction of the solar spectrum.
- High intensities of light cause heating in solar cells. Hot silicon is less efficient than cool silicon, but a heat dissipator can help this problem.
- These systems are impractical for incorporation into architecture.

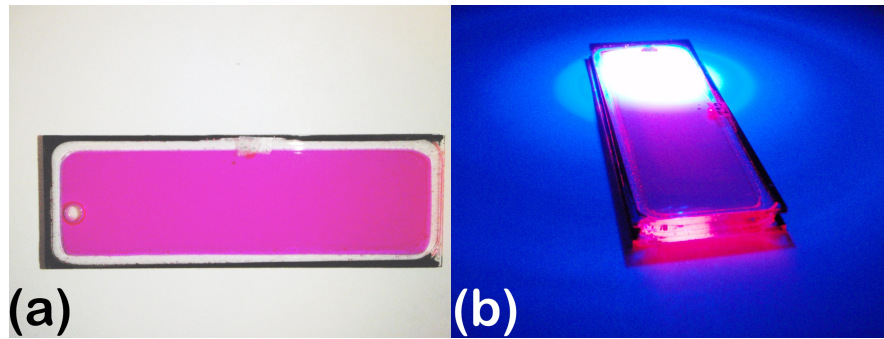


Figure 2.1: Luminescent solar concentrators constructed from microscope slides(a). Under illumination (b), light is guided to the edge of the concentrator.

Luminescent solar concentrators (LSC's) employ the simplest physics to correct all of these problems. Figure 2.1 depicts LSC's constructed from microscope slides. Simply put, an LSC is a flat glass box filled with a highly fluorescent absorber; the simplest absorber is a fluorescent dye dissolved in solvent. When light shines into the LSC through the large face, it is absorbed inside the concentrator then re-emitted at random angles. Ideally, the light will be emitted at some longer wavelength outside the absorption bandwidth of the absorber, so that the absorber will become transparent to the freshly emitted photon. This shift in photon energy is known as a Stokes shift, and it will be discussed later. Some light will immediately exit the concentrator again through one of the two large faces, and some will be trapped inside the concentrator by total-internal reflection and waveguided to the edge.

In order to effectively concentrate light, a large number of photons must be trapped inside the concentrator. 10% power efficiency is a good rule of thumb for a commercially viable solar cell. The most efficient solar cells, which will line the edges of our LSC, are only around 30% power efficient, so capturing a bit over 30% of the

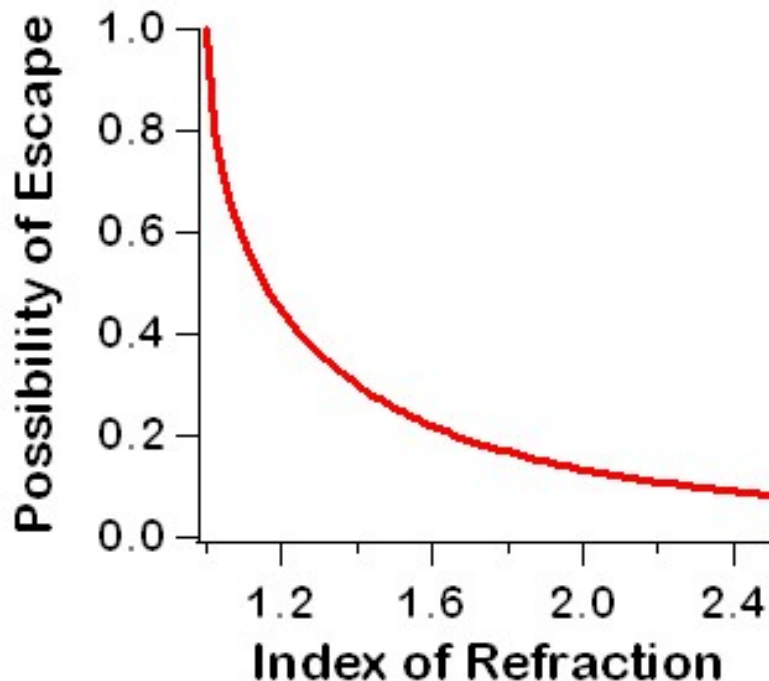


Figure 2.2: A plot of $1 - \frac{\sqrt{n_2^2 - 1}}{n_2}$. Solvent indices are around 1.4.

photons available should yield around 10% overall LSC power efficiency. Using Snell's law, $n_1 \sin(\theta_1) = n_2 \sin(\theta_2)$, and the back of a convenient envelope, one can calculate the expected fraction of randomly emitted photons that would escape through the large faces of an LSC surrounded by air ($n_1 = 1$) as $1 - \frac{\sqrt{n_2^2 - 1}}{n_2}$, which is plotted in figure 2.2. Typical n for solvents are around 1.4, which means around 70-75% of photons emitted by the absorber will be forced to escape through the narrow edge of the LSC.¹

The real trick is in the choice of absorber. A material must be transparent to the emitted photons to be effective as an LSC material; otherwise, emitted photons

¹This assumes the glass index of refraction matches that of the solvent. The calculation is merely intended to illustrate the effectiveness of this technique for trapping photons.

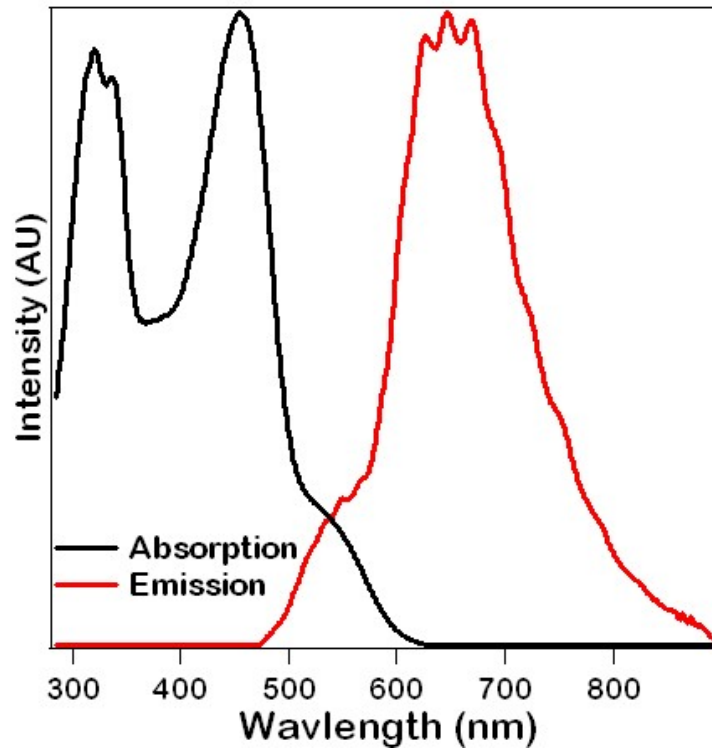


Figure 2.3: Normalized absorption and emission spectra from a red poly-fluorine in chlorobenzene. The difference in wavelength/energy from peak absorption to peak emission is known as a Stoke’s shift—150nm in this case.

would continually be reabsorbed and emitted in a new random direction, until finally the photon is emitted at an angle that would allow it to leave the concentrator. This absorber transparency is accomplished via what is known as a Stoke’s shift—an offset between absorption and emission spectra. (See figure 2.3.) Stoke’s shifts can be many tens of nanometers in wavelength, and a large Stoke’s shift is critical for LSC absorber materials.

Given perfect absorber transparency at fluorescence wavelengths, one could coat the edges of the LSC with mirrors and connect an arbitrarily small photodetector

on the LSC to gather the photons and convert them to power. Since the photons are trapped, the size and location of the detector are irrelevant; eventually, every photon will find it's way to the detector. Unfortunately, the Stoke's shift for most materials isn't enough to escape loss from the Urbach absorption tail, and many other loss mechanisms in this innocent little system quickly pile on to the point where an exact solution becomes impractical, and computer simulation must be employed to determine if LSC's are viable.

2.1 Computer Simulation of LSC

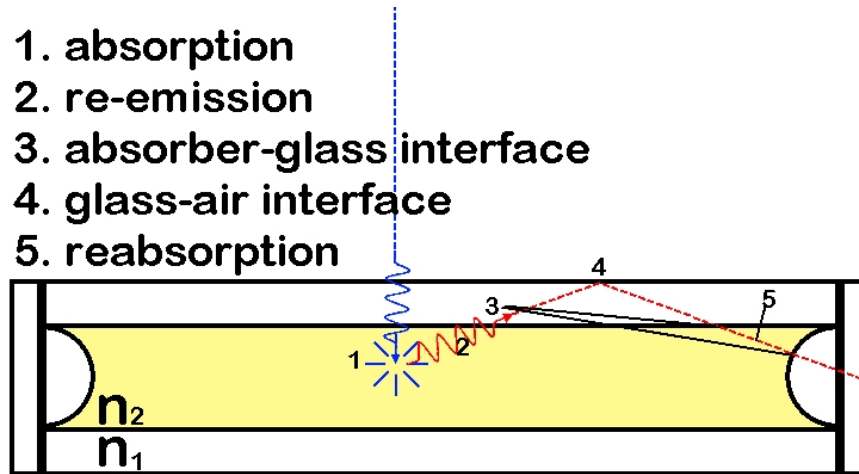


Figure 2.4: Depicted are basic steps in our Monte-Carlo simulation. n_1 and n_2 are indices for the glass and solvent, respectively. A photon enters the LSC and we test for absorption (1), then re-emission (2). We determine a trajectory and allow the photon to proceed through the LSC step-wise, checking for reflection at each interface (3), until it leaves the LSC. Reflections at (4) are guaranteed by total internal reflection. Photons will be reabsorbed (5) at a pre-determined distance based on the absorption coefficient for the new wavelength.

To determine optimum material parameters, we created a Monte-Carlo simu-

lation of our experimental LSC's. Our chief concern at the time was calculating photon loss as a function of the LSC boundary geometry. Look again at figure 2.1; we sealed the microscope slide edges using a bent glass rod, with the diameter of the rod defining the thickness of the LSC. Our first concern was that the round glass-solvent interface at the edge of the LSC might be a large reflective/refractive light loss, and we wished to optimize the interface geometry, and determine which other light losses were most significant.

To simulate an LSC, first, the LSC geometry and absorber emission/absorption spectra are defined. Figure 2.4 depicts the basic steps used in our simulation; further details are available in B.1. Photon are generated one at a time and allowed to “shine” onto the collector. Each photon is assigned a wavelength with a distribution matching the solar spectrum. After checking for reflection at each interface, the photons have an opportunity to be absorbed. Absorption probabilities we determined employing the Beer-Lambert law,

$$I(l) = I_0 e^{-\alpha M l}$$

where $I(l)$ is local light intensity, I_0 is initial intensity, l is the distance the photon has traveled in the absorber, M is the molar concentration, and α is a measured absorption coefficient. (Absorption coefficients are linearly proportional to the number density of absorber molecules, so any measure of absorber concentration, such as grams per liter, may be used in place of molarity provided those units were used to determine

α .) I/I_o is fractional transmitted light, so the probability of absorption becomes simply

$$1 - e^{-\alpha M l}$$

Once absorbed, a photon may be emitted in any direction. There is no guarantee of emission; the probability of emission is known as the fluorescence quantum yield (ϕ_f). (The measurement of this will be discussed thoroughly in A.3.) Once a test is passed to emit a new photon, we assign a new direction randomly. A new wavelength no shorter than the original photon's wavelength is also assigned according to our measured emission spectrum.

The photon is then allowed to proceed step-wise through the LSC. At index boundaries, the photon is allowed an opportunity to reflect based upon reflectivity coefficient, and, failing reflection, the photon refracts into the next medium.

Eventually, a photon will be reabsorbed by the medium in much the same manner it was absorbed in the first place. (This will be discussed in detail in section 1.4.2.) Look again at figure 2.3. Despite the 150nm Stoke's shift, there is significant overlap between the emission and absorption spectra of this particular material even at wavelengths longer than 600nm. To reabsorb, we randomly pre-determine a distance (l_{abs}) the photon will travel in the absorber using $l_{abs} = -\ln R_{an}/(\alpha M)$. R_{an} represents our randomly generated number between 0 and 1.

Each LSC's emission spectrum will be unique. To a poor approximation, the LSC emission spectrum will merely be the material's emission, but the overlap between absorption and emission will change the spectrum significantly as will be seen. Since

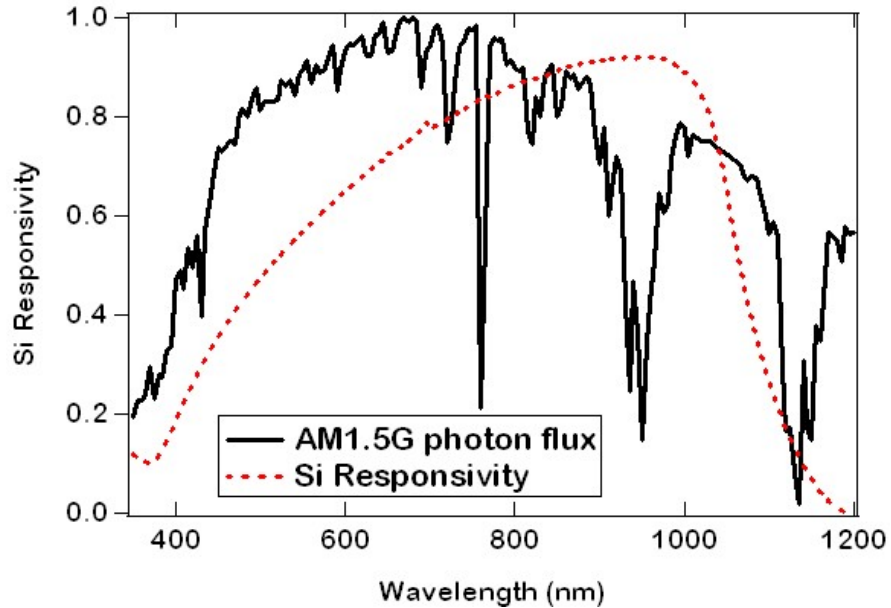


Figure 2.5: AM1.5 Global photon flux density standard and silicon responsivity plotted together. Notice that silicon's reponsivity is 30 – 50% lower at visible wavelengths than at near-IR wavelengths.

the responsivity of silicon is changing rapidly in the visible wavelengths, as can bee seen in figure 2.5, it is not enough to count the photons collected. Our materials emit at varied positions in the visible spectrum. A shift from 500nm to 600nm would mean an increase in silicon EQE from 50% to 60%....that's a 20% increase in measured current! To have something to compare with experiment, we must calculate expected currents using the technique described in A.2.1.

These steps more or less complete the simulation. A new photon generates once a photon fails to absorb, fails to be re-emitted, or leaves the LSC either through any face. By counting the photons escaping through various routes, we can predict which loss mechanisms dominate our LSC's and determine which parameters dominate

these losses. Incoming light can be easily redefined to match experimental conditions; for example, a small area through which incoming photons must enter can be defined to simulate a mask or small-area light source, or all incoming photons can be assigned one wavelength to represent a laser. And, most importantly, we can simulate actual currents expected from these devices and predict what materials and geometries would be required for an efficient, commercially viable concentrator.

2.2 Loss Mechanisms in LSC's

The simulation established quickly that reflective/refractive losses because of edge geometry were minimal, and other losses were much more important. The first major loss mechanism in an LSC is failure to absorb a given photon. Dyes for LSC's are typically dissolved organic materials, like polymers or small-molecules. Their absorption spectra are confined to a few hundred nanometers of the visible spectrum. Since silicon's bandgap is 1.1eV, the photons of interest extend from 350nm to 1100nm in wavelength; a single dye will not absorb most of the available solar spectrum. Absorption for any given absorber is easily measurable with a spectrometer.

Once a photon is absorbed, it must be re-emitted. Excited electrons can decay thermally, and, in general, every photon absorbed will not be re-emitted. The fraction of absorbed photons emitted is known as fluorescence quantum yield (ϕ_f), and it is roughly independent of excitation wavelength [94]. For an LSC absorber, ϕ_f should be as close to unity as possible; 30% or so of photons will be lost due to the index of

refraction limits of available solvents. ϕ_f values below .5 immediately drop collection efficiency to the limit of 30% photon collection, and absorption bandwidth limits are going to reduce photon collection further still. The measurement of this quantity will be discussed in detail in A.3.

One loss mechanism has already been introduced—failure to trap light through total internal reflection. Of course, the actual fraction of photons trapped by an LSC is not as simple as depicted in figure 2.2, and is not easily calculated on paper. The actual fraction will depend upon the index of the solvent as well as the index of the glass. What’s more, even if all of these data are wrapped up into one neat equation, this calculation would ignore the possibility of re-absorption in the absorber layer; this possibility is material dependent. Numerical calculation is more practical.

Overlap between the absorption and emission spectra provide another loss-mechanism, although somewhat indirectly. Once a photon is trapped, re-absorption is highly undesirable. Any time a photon is absorbed, it’s chance to be lost immediately is roughly the product of ϕ_f and the fraction of solid-angle trapped by total-internal refraction. For $n = 1.5$ and $\phi_f = .7$, the chance to be lost is around 50%! Because of the geometry of LSC’s, the overlap between absorption and emission spectra is more significant than might be immediately apparent.

To absorb a photon as it travels through the LSC initially, the concentration should be varied such that the absorption $(1 - \frac{I(l_o)}{I_o})$ approach unity within the material’s absorption bandwidth to optimize absorption of the solar spectrum. l_o is the LSC thickness. Absorption should also approach zero for the emission wavelengths to mini-

mize reabsorption of fluoresced light. But the relevant distance for the re-absorption is no longer l_o .

Geometric gain from an LSC we'll define as $G_{geo} \equiv A_{col}/A_{conc}$, where A_{col} is the area of a collection face, and A_{conc} is the area the light is concentrated onto. If the LSC is to be useful in any way, the geometric gain should be large. A_{conc} we'll approximate with $l_o \cdot l_{trvl}$; l_{trvl} is the average distance a photon must travel to reach the collector edge, and l_o is the LSC thickness. Similarly, we'll approximate A_{col} with l_{trvl}^2 . So the geometric gain should be approximately equal to $\frac{l_{trvl}}{l_o}$. This value is around sixteen for our experimental devices. We've defined the geometric gain this way to locate an important wavelength λ^* . Using Beer-Lambert again, we can find

$$e^{\alpha(\lambda^*)Ml_oG_{geo}} = 1/2$$

This defines λ^* , which will lie in the emission spectrum of the absorber. The significance is that roughly half of the photons emitted at wavelength λ^* will be re-absorbed before reaching the edge of the concentrator, and will likely be lost from non-radiative recombination or emission at an angle less than θ_{crit} . Fortunately, thanks to the exponential distribution of trap states within the band-gap [40], the absorption coefficient α falls exponentially at the absorption edge, while G_{geo} need only be around 100-1000. But even materials with a large Stoke's shift typically have λ^* somewhere inside the emission bandwidth. (This can be seen in table 2.2 in section 2.3.)

One perhaps unexpected loss of efficiency will arise from geometric and transmissive losses in the glass. A sheet of glass will have some color when viewed from

the edge because the glass, like the absorber, has an absorption spectrum, obviously with a much smaller amplitude.² Most glass will have a blue-green tinge, however, so the absorption favors red light, which will absorb our emission spectrum. This is expected to be a significant consideration for large-area LSC's, but we'll ignore it for our simulations.

Another consideration for large-area concentrators is LSC face alignment. A poorly constructed concentrator will allow trapped light to escape, as shown in figure 2.6. Pictured are two glass sheets misaligned by some angle δ . As a photon reflects inside the LSC, it's trajectory will adjust by δ after each reflection. Since a photon will undergo many reflections as it travels to the LSC edge, it's important that $N \cdot \delta$ be very small relative to θ_{crit} , where N is an average number of reflections a photon will undergo.

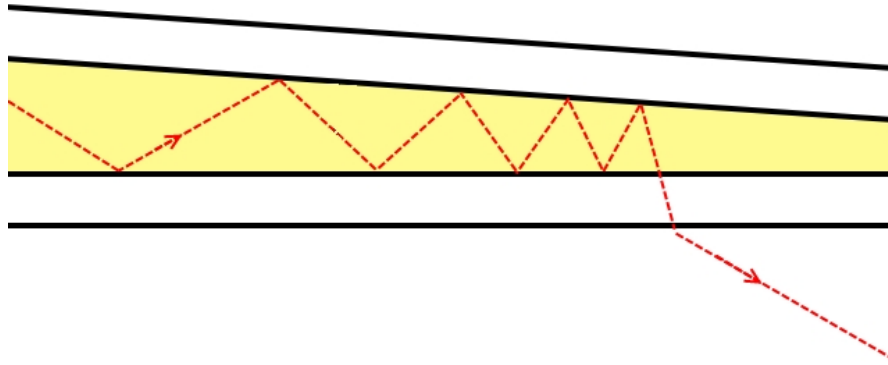


Figure 2.6: Misaligned LSC faces will eventually guide a photon out of the concentrator.

²This is a simple experiment to do. Take a sheet of glass, place it edge-wise against a white sheet of paper. Observing carefully, you will see the top edge brighten as diffuse light from the paper is waveguided through the glass.

2.2.1 Measuring a small absorption coefficient

For a non-fluorescent material ($\phi_f \ll 1$), measuring a small absorption coefficient is straightforward; examining Beer-Lambert's law and our geometric gain G_{geo} , our molarity of interest is only 1000 times greater than the collector's molarity, and this is often achievable for a good absorber. However, LSC's require materials with high fluorescence. The wavelengths that we wish to know the Urbach absorption are the fluorescence wavelengths; an attempt to measure absorption directly will need to separate fluoresced light from transmitted light. If the fluoresced spectrum and transmitted light are comparably bright, this will be challenging.

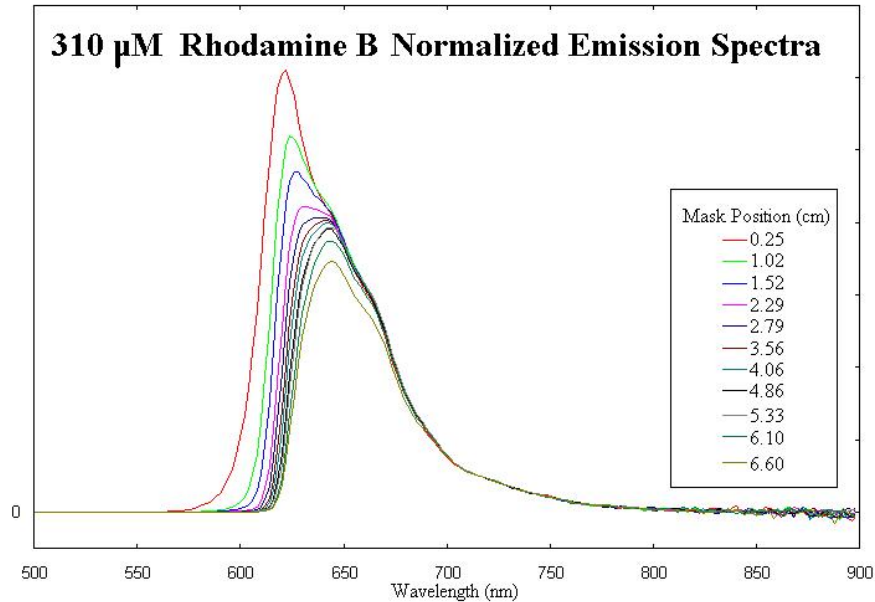


Figure 2.7: Spectra emitted from the side of a LSC redshift as the light source moves farther from the detector due to overlap between the absorption and emission spectrum. Once normalized, the spectra provide intensity datapoints as a function of distance, and can be fitted to Beer-Lambert to find absorption coefficients.

We have employed an alternate technique to measure the absorption in this

troublesome region; we measure the redshift of a fluoresced spectrum. Look at figure 2.7. A spectrometer recorded spectra at the edge of an as a function of distance to a light-source. Although the amplitudes will be a complicated convolution of geometric effects, including solid-angle and reflection off the side-walls, these can be eliminated by assuming that the absorption coefficient at longer fluoresced wavelengths (700nm for this example) is much smaller than the absorption coefficients at the short-wavelength fluorescence. By forcing fluorescence to have the same intensity at long wavelengths, we have effectively isolated absorption processes from geometric effects. With these geometric effects removed, we can treat these spectra as transmitted through various thicknesses of absorber. Since our LSC's are only a few centimeters long, each LSC can only measure a narrow band of redshift and thus a narrow window of absorption coefficients. But one can extend the utility of this technique by fabricating several LSC's of varying concentrations. Figure 2.8 depicts absorption coefficients measured for RhodamineB in this manner. Notice that the absorption coefficient has been measured out to 670nm. The absorption coefficient drops exponentially in this range, although it is not well-fit by a single exponential. This provides a good estimate of our absorption coefficient well beyond the limits of our transmission spectrometer. Our smallest measured absorption coefficient is more than four orders of magnitude smaller than the peak absorption for Rhodamine B, and the absorption spectrum has been extended nearly to the end of the emission spectrum. (Refer to figure 2.3.) This technique does make several assumptions; it assumes the light is essentially collimated, travels only in the absorber, and does not re-fluoresce after re-absorption. Of course, the light is not

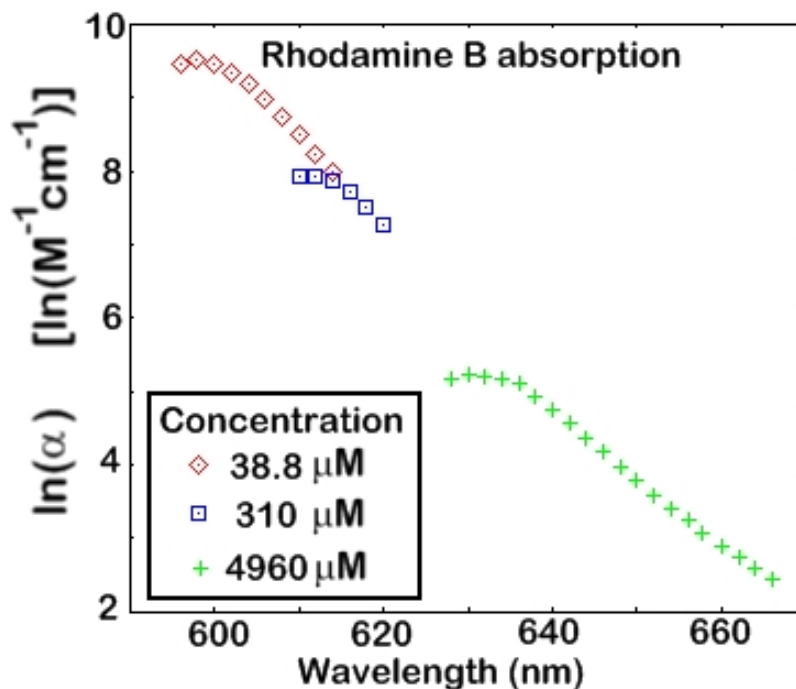


Figure 2.8: Absorption coefficients measured by observing the redshift of LSC emission spectra as the light-source becomes more distant from the photodetector. Three concentrations of absorber were used; each concentration produces a narrow band of useful data for a given geometry.

collimated; the path length l is longer than just the distance from the light-source to the detector. Diffuse light will reflect off faces as it travels to the detector, and some average path length should be used to calculate absorption. However, the light will not travel exclusively in the absorber. Since the index of the glass is close to the index of the solvent, the light will spend a significant portion of its travel in the glass; this will tend to reduce the effective path length, so these errors will act to counteract each other to some extent. There was no obvious solution to these shortcomings, but all of these corrections should be of order one, while the absorption is dropping exponentially, so

we should be able to safely ignore these problems.

2.3 Simulation Results

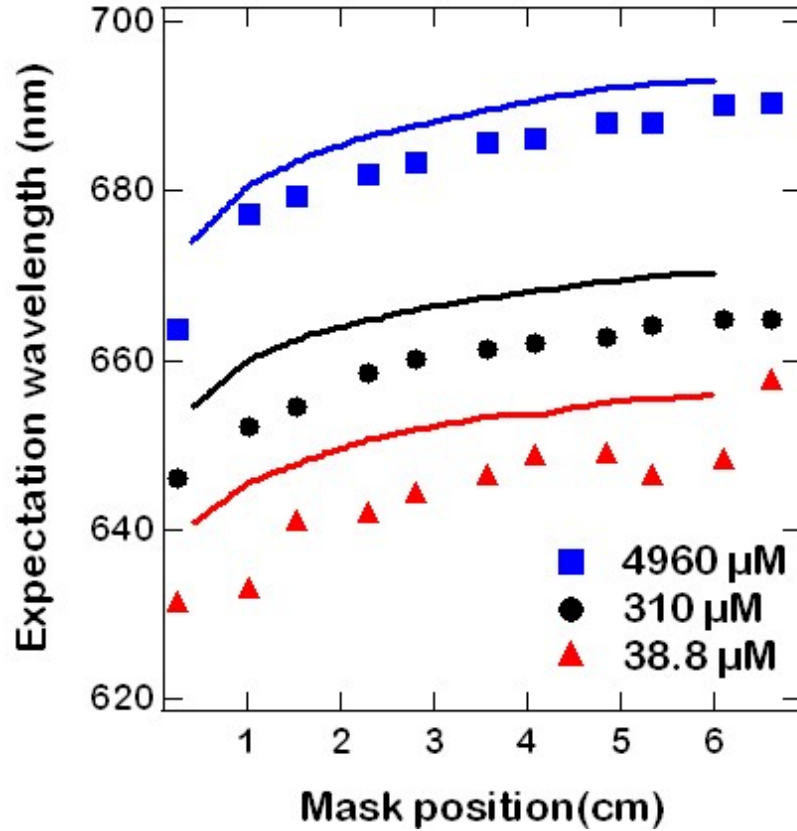


Figure 2.9: Expectation values (λ_{exp}) for emission spectra as a function of mask position. Traces are simulated values, and shapes are experimental.

First, to verify that the simulation was working properly, spectra were generated as a function of distance from mask to detector. Quantitative comparison could be made by calculating a wavelength expectation value λ_{exp} :

$$\lambda_{exp}(d) \equiv \frac{\int \lambda \cdot I(\lambda, d) d\lambda}{\int I(\lambda, d) d\lambda}$$

Figure 2.9 shows the expectation values for three LSC's filled with various concentrations of Rhodamine B. The simulation accurately predicts the size of the spectral redshift, although the expectation values are offset by 10-20nm from experimental spectra.

Simulated power conversion efficiencies provide a better sanity check on simulation data; table 2.1 shows our measured ϕ_f values, experimental collection efficiency (η_{exp}), and simulated currents at the detector in milliamps for the best performing LSC of each material studied. η_{exp} we'll define as

$$\eta_{exp} \equiv \frac{I_{edge}}{I_{detector} \cdot G_{geo}} \propto I_{edge}$$

$I_{detector}$ is the current measured at a one-inch edge of our 1" by 3" microscope slides, and I_{edge} is the current measured using direct illumination of the silicon detector placed at the edge of the concentrator. η_{exp} defined this way is a somewhat meaningless number except for comparison to other materials. It's not an actual efficiency of photon collection; it's a 'current concentration' efficiency. Since the currents generated result from different spectra, and the detector's response is spectrally dependent, the current ratios aren't equal to the photon collection ratios. But η_{exp} is directly proportional to current at the edge, which is all we really care about as long as the simulation is generating the expected spectrum at the collector's edge.

The correlation between all simulated currents and experimental LSC currents is shown in figure 2.10. Experimental and simulated currents correlate reasonably well ($\rho(I_{sim}, I_{exp}) = 0.862$), although there is a large disparity. Taking the simulations and

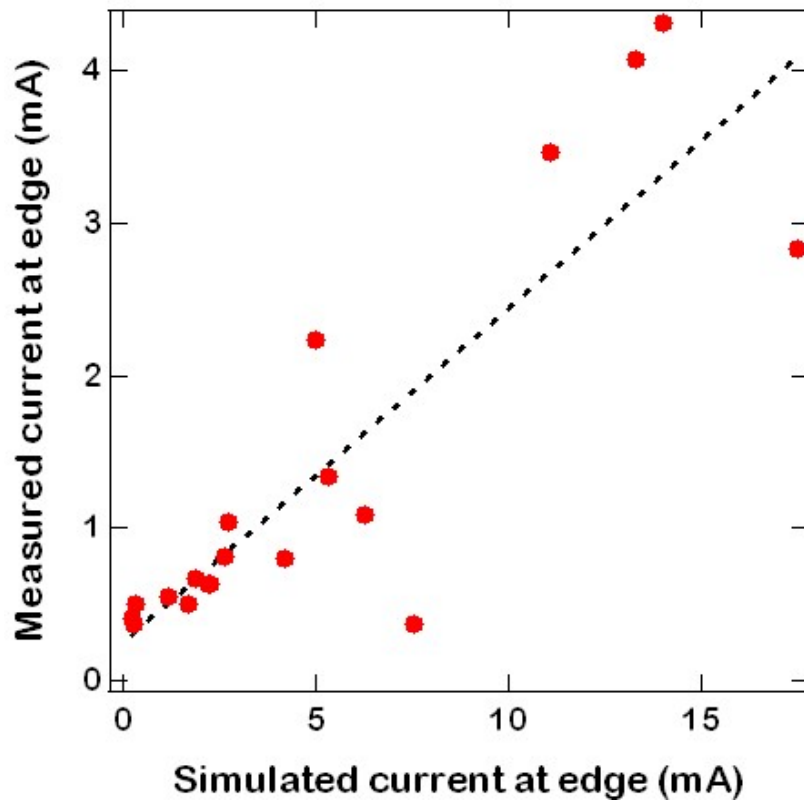


Figure 2.10: Correlation between experimental collection efficiency and simulated current expectation. These are expected currents at full 100 mw cm^{-2} illumination. The correlation coefficient is 0.828.

experiments at face-value, roughly 70% of the photons the simulation accounts for are lost in experimental LSC's.

The simulation results can only be as accurate as the (difficult) ϕ_f measurement, so even if there are no significant losses in the LSC's other than those being simulated, a near unity correlation is not expected. The absolute ϕ_f of Rhodamine B in polyethylene-glycol may be smaller than 0.95. Although it was clearly more fluorescent than other materials measured, the near unity fluorescence typical of Rhodamine may not apply in such a viscous solvent.

Table 2.1: ϕ_f , measured efficiencies, and simulated currents for our LSC's. Experimental intensities are about half of AM1.5G...the simulation's intensity was matched to mimic the experiment. Expected current under full $100mWcm^{-2}$ scale accordingly.

| Absorber | $\phi_f(\%)$ | $I_{exp}(\text{mA})$ | $I_{sim}(\text{mA})$ |
|-------------------------|--------------|----------------------|----------------------|
| Rhodamine B (dye) | 95 | 1.87 | 6.0 |
| Red polyfluorine | 67 | 2.33 | 7.56 |
| MEHDOO (C60 polymer) | 48 | 0.59 | 3.38 |
| MDMO (C60 polymer) | 45 | 0.72 | 2.88 |
| LDS698 (dye) | 11 | 0.44 | 1.43 |
| LDS821 (dye) | 9 | 0.36 | 1.02 |
| CdSe/ZnS (nanoparticle) | 7 | 0.2 | 0.15 |

Having made some measure that the simulation is performing as expected, we can begin to make predictions. Examine table 2.1. It is clear that a high value for ϕ_f is critical for an effective LSC. ϕ_f is dependent upon solvent, temperature, and material purity [24], so the values we measured may or may not be the limit for these materials. To explore the importance of other material properties, we would like to eliminate ϕ_f as a variable. ϕ_f will be set to unity for all materials, and we can measure the dependence of our concentrators on other material properties such as Urbach absorption tail and spectral overlap and attempt to predict what other material properties are important to produce a useful LSC.

Table 2.2 shows expected power efficiencies for simulated LSC's with $\phi_f = 1$. For these, the geometric gain was set to $33\frac{1}{3}$. With this geometric gain, and a square area of one meter, the fraction of silicon required for collection over this area will be $\frac{4}{33\frac{1}{3}}$, which is about 12%. This is a minimum of cost reduction from less silicon. Really, we'd like to push the geometric gain higher, but the Urbach absorption will reduce the efficiency as G_{geo} becomes large. So by examining efficiencies at this G_{geo} ,

Table 2.2: Simulated collection efficiencies (η) with ϕ_f set to unity. η was calculated using a silicon detector fill-factor of 0.7 and a V_{oc} of 1V. This is simulated at a minimum practical G_{geo} to reduce losses from Urbach absorption.

| Absorber | $Emit_{range}$ | λ^* | η |
|------------------|----------------|-------------|--------|
| Rhodamine B | 570nm–720nm | 649nm | 6.1% |
| Red polyfluorine | 500nm–800nm | 625nm | 8.4% |
| CdSe/ZnS | 580nm–660nm | 662nm | 4.5% |
| LDS821 | 700nm–920nm | 808nm | 12.8% |

we can eliminate materials whose properties are too poor for LSC use before Urbach absorption becomes a significant problem. $Emit_{range}$ spans the wavelengths that the material fluoresces in, and λ^* is the wavelength at which the absorption coefficient will be $\frac{1}{2}$, for comparison.

We are also interested in how high we can push the geometric gain G_{geo} . High geometric gain will reduce the amount of required silicon and redshift our emission spectrum to better match silicon’s responsivity. But as the emission spectrum is redshifted, much of it will be lost to geometry or ϕ_f , as some significant fraction of photons emitted will not be trapped/fluoresced. We will adjust the thickness of the LSC and the concentration of the absorber such that $\alpha M l_o$ remains constant.

There is a limit to how high we’re interested in pushing the geometric gain. l_o is only the thickness of the absorber layer. The photons will travel in the glass, so the silicon detector will have area proportional to the glass thickness plus the absorber thickness. Once the absorber layer is significantly thinner than the glass, no further significant cost reduction can be made by making the absorber layer thinner, so the geometric gain has a practical lower bound. A practical device will have glass thicknesses

of a few millimeters, so a one millimeter thick absorber layer is about as thin as we're interested in. Similarly, the geometric gain has a lower bound; a geometric gain of four, for example, would mean that the area of the silicon detector at one side would be $\frac{1}{4}$ of the area of the LSC face. The total silicon detector area is equal to the LSC front face, and our LSC will cost more money to fabricate than a standard silicon solar panel. So we'll examine geometric gains between ten and ten-thousand—LSC faces of one square meter and anywhere from 10cm to 1mm thick.

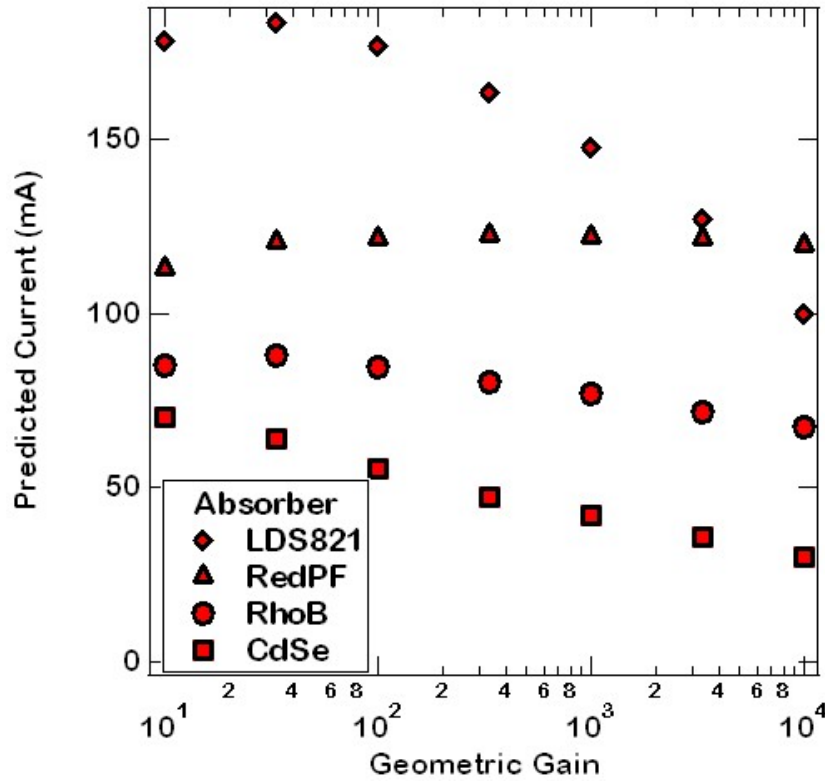


Figure 2.11: LSC performance as a function of G_{geo} . For these simulations, ϕ_f was set to one.

No single parameter explains the results here, but examining the spectra ex-

plains everything. Figure 2.12 has spectra for LDS821 laser dye and CdSe nanocrystals. Red polyfluorine spectra are in figure 2.3, and Rhodamine spectra are in figure 1.9. LDS821 has a very broad absorption and a good Stoke's shift, but the Urbach absorption becomes problematic for large G_{geo} . The red polyfluorine doesn't absorb nearly as far as LDS821, but it has a good Stoke's shift and the smallest Urbach coefficient in this group, so its performance doesn't degrade as G_{geo} increases. Rhodamine B has a similar absorption, a reasonable Stoke's shift, so its performance at low G_{geo} is poor. It also has a moderate Urbach coefficient, so it suffers as G_{geo} increases. CdSe nanocrystals suffer from having essentially no Stoke's shift; light collection is due mostly to light incident near the edge of the LSC, as these photons will have a short path length.

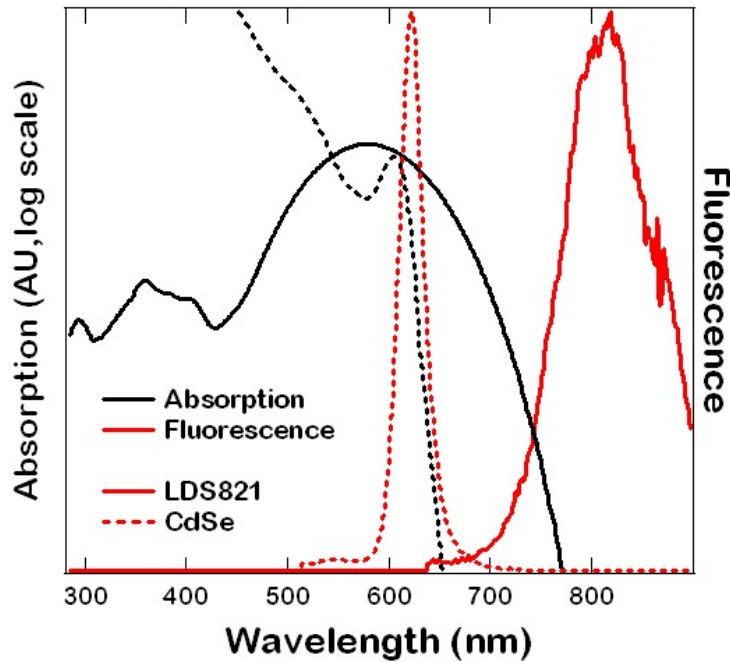


Figure 2.12: Fluorescence and absorption for LDS821 laser dye, and CdSe nanocrystals. Absorption displayed on a log scale to show the beginning of the Urbach absorption tail.

2.3.1 Urbach absorption: open questions

One question critical to this simulation remains fundamentally unanswered.³ Do photons absorbed from the Urbach absorption tail result in fluorescence? If so, at what wavelength, and with what efficiency?

In general, excitation at wavelengths above the bandgap result in the same fluorescence spectrum, without regard to the excitation wavelength. However, the physics are fundamentally different for Urbach tail absorption. If there are enough free charge carriers, it may be that an electron excited into a trap state can relax into an open position in the valence band. In this case there's no reason to conserve energy—the photon emitted will necessarily be more energetic than the one absorbed. But it's also possible that the trap states are due to local defects, in which case relaxation may be a local process, and our excited electron is destined to return to the trap state from whence it came, and energy will be conserved. And there's *no* justification for assuming that the ϕ_f is the same for photons with more and less energy than the bandgap.

The most optimistic assumptions would actually be energy conservation and matching ϕ_f . This *could* be the case for localized defects in the energy spectrum. Assuming energy conservation excludes the blue side of our material's fluorescence spectrum, which means that absorbed photons will always be red-shifted. Our materials absorb in the blue, and silicon is most efficient in the infra-red, so the more red-shifted our collected light becomes, the better. Additionally, red-shifted light becomes exponentially less likely to become reabsorbed and hazard loss via ϕ_f or emission at a non-trapped

³At least as far as the author has been able to discover.

angle.

The only slightly less optimistic assumption would be that fluorescence is just as efficient, but energy is not conserved, so fluoresced light can be emitted anywhere from the fluorescence spectrum with no regard to the excitation wavelength. This could occur if a trapped electron is excited into the LUMO band, then relaxes quickly into a nearby hole in the HOMO band. This set of assumptions is much less realistic. A ‘large’ number of charge carriers would be between 10^{16} – 10^{19} cm^{-3} , but there are around 10^{22} ions cm^{-3} . So the odds of a vacancy existing close to the excited electron are low, and this would be required for ϕ_f to be the same.

This brings us to the last and most restrictive assumption: Urbach absorption must be counted as loss. More precisely, we can assume that ϕ_f is energy dependent, being small for photons with less energy than the bandgap. Since we have been assuming that ϕ_f is unity, the simplest assumption is that the sub-bandgap photons have not chance of fluorescing. We have no measure of which of these scenarios is most likely; over the distances we have measured physically, the Urbach absorption is fairly small. It’s not easy to decide exactly where Urbach absorption *should* begin. By the symmetry of figure 2.3, one can see a regime of absorption and emission that appears inverted, as if the rules for Franck-Condon apply but the emitted photon is more energetic than the absorbed photon somehow.

We can at least measure the consequences for these scenarios via simulation. The results of our simulations can be seen in tables 2.3 and 2.4. The two assumptions used were that energy was conserved and ϕ_f did not change (“Urbach PL”), or that there

Table 2.3: Comparison of simulated and experimental currents. Reported currents are at one edge of the LSC, and represent approximately $\frac{1}{7}$ of the total current expected. ϕ_f was set to measured values for comparison with experiment.

| Absorber | Urbach PL Current (mA) | No Urbach PL Current (mA) | Experimental Current (mA) |
|-------------------|------------------------|---------------------------|---------------------------|
| Rhodamine B | 11.3 | 4.1 | 3.5 |
| Red polyfluorine | 13.6 | 11.1 | 4.3 |
| CdSe nanocrystals | 0.24 | 0.17 | 0.37 |
| LDS821 | 1.8 | 1.8 | 0.41 |

was no fluorescence from the Urbach tails (“No Urbach PL”). This second assumption is non-trivial to define for these materials, as noted above. As such, we defined any absorption of a photon after it’s initial absorption as an Urbach absorption.

Looking first at table 2.3, simulated currents showed little difference between the two assumptions, with the exception of Rhodamine. This makes sense, as there is expected to be little re-absorption in this geometry, with the exception of Rhodamine. One might protest that the numerical agreement between Rhodamine is much better by assuming that there is no fluorescence from re-absorption, so this must be the correct assumption and the cause of the large numerical disparity between simulation and experiment. However, since this is *only* true for Rhodamine, the more likely reason for this agreement is that we are defining ‘Urbach’ absorption too strictly for Rhodamine, which has significant spectral overlap relative to the fluorescence bandwidth, and that the losses resulting from this happen to match up roughly with the losses the simulation hasn’t accounted for.

Now let us examine table 2.4. This table summarizes the results for simulations of small and large G_{geo} concentrators. For all materials, the assumption of zero ‘Urbach’

Table 2.4: Effects of extreme cases of Urbach photoluminescence for small and large G_{geo} .

| Absorber | $G_{geo} = 33.3$ Urbach PL $\eta(\%)$ | $G_{geo} = 1000$ Urbach PL $\eta(\%)$ | $G_{geo} = 33.3$ No Urbach PL $\eta(\%)$ | $G_{geo} = 1000$ No Urbach PL $\eta(\%)$ |
|-------------------|---|---|--|--|
| Rhodamine B | 6.0 | 5.5 | 2.0 | 0.84 |
| Red polyfluorine | 8.4 | 8.6 | 5.5 | 4.7 |
| CdSe nanocrystals | 4.5 | 3.0 | 0.57 | 0.07 |
| LDS821 | 12.8 | 9.9 | 8.4 | 2.4 |

photoluminescence was catastrophic at large geometric gain. The notable exception to this was the red polyfluorine, which had a very small Urbach coefficient. But for reasonable G_{geo} , even assuming no photoluminescence from reabsorbed photons yields a reasonable power efficiency from LDS821. Unfortunately, this was done assuming the ϕ_f for this material to be 1, not 0.09, as was measured. So this particular dye will not suffice for implementation in an LSC, but perhaps a material with similar properties will suffice.

2.4 Conclusion

We have seen that the predicted efficiency of our luminescent solar concentrators is dependent primarily upon the fluorescence efficiency of the absorber ϕ_f , and secondarily upon the amount of spectral overlap between absorption and fluorescence. The size of the band-gap is also critical; assuming good fluorescence, the materials with the smallest band-gaps performed best for moderate G_{geo} . Urbach absorption is only expected to become important for large G_{geo} , although, to be competitive with the

silicon PV industry, large G_{geo} may be necessary. A large disparity exists between experimental and simulated concentrators; this is attributed to red absorption in the glass and imprecise measure of ϕ_f .

However, the requirements for a material to make a reasonably power-efficient are actually not too demanding. All that is needed is a highly fluorescent material with a band-gap around 1.1-1.5eV, good spectral separation between fluorescence and absorption⁴, and a solvent/glass with indices around 1.5 and high transmission over a meter. Given that much of our communication currently depends upon fiber-optic cables that transmit light many kilometers, and new small-bandgap conjugated polymers are being discovered/engineered at a high rate, these requirements seem achievable in the near term.

⁴The LDS821 spectrum in figure 2.12 is an example of what is ‘good’ separation

Chapter 3

Bulk Heterojunction solar cells

3.1 Introduction

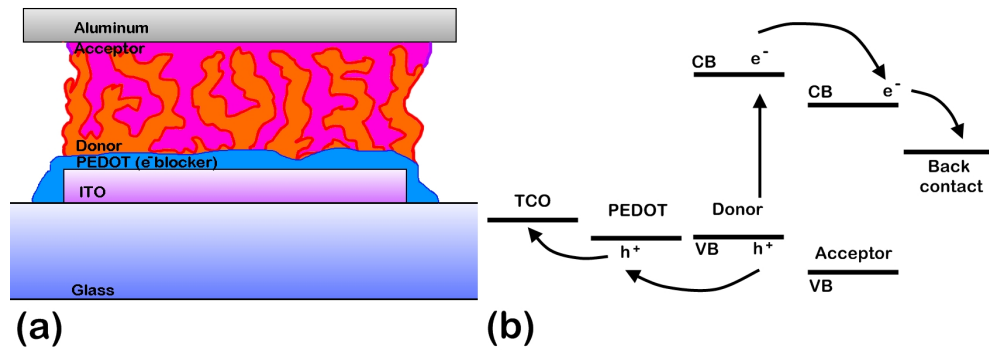


Figure 3.1: Device structure(a) and transport(b) for a bulk heterojunction solar cell.

Bulk heterojunction photovoltaics are explained most easily by examining their name. A heterojunction is a device made from different semiconducting materials. Silicon photovoltaics are homojunction devices. ‘Bulk’ means that the junction is not confined to a plane, but instead is found throughout the bulk of the photoactive layer.

Figure 3.1 depicts a typical bulk heterojunction (BHJ) cell. By blending the donor and acceptor phases, the entire thickness of the BHJ absorber becomes an energy junction.

The purpose of this becomes clear once the physics are understood. When a semiconductor absorbs a photon, an electron-hole pair called an “exciton” is formed [19]. The exciton has two easily understood properties with immediate consequence. First, it is a neutral particle, as it consists of an electron and a hole. Second, it can be broken into an electron and a hole, but this requires energy. For polymers, this energy is usually around 100 meV or more [12].

Excitons are not unique to semiconducting polymers and quantum dots. Inorganic semiconductors can also have excitons, but the exciton binding energy is now going to be less than the thermal energy [92], so the excitons are quickly split. Consequently, although the physics differ only in degree, the behavior of inorganic and organic semiconductors is completely different at room temperatures.

The tightly bound exciton is the reason for the complex structure. The exciton cannot split until it finds the energy needed to overcome the electron binding energy. Since lattice vibrations are insufficient, it must find a boundary between the donor and acceptor phase, so the electron can relax into the acceptor phase, or the hole into the donor phase. Because the exciton is neutral, it is unresponsive to electric field, and must diffuse to a boundary. An exciton will diffuse around ten nanometers before recombining [55]. To maximize exciton splitting, the phase separation should have a typical length scale of ten nanometers. (See 1.2.2.)

There is a problem with this, however. Once an exciton is split, the free carriers

must have a phase-continuous path to their respective electrodes. This isn't easy to engineer. Without deliberate phase structuring, the thickness of the film should be similar to the scale of phase separation; as the phase separation becomes finer and finer, given the same film thickness, the likelihood that islands of one phase or another will form that have no electrical connection to their electrodes increases. Photons absorbed in these islands will act as traps for charges, reducing carrier collection and transport properties.

Typical thicknesses for BHJ films are around 100-200 nanometers. All available light isn't typically absorbed over this distance, but these thicknesses are necessary for carrier extraction; mobilities are low in polymer films, around $10^{-4} \text{cm}^2 \text{V}^{-1} \text{s}^{-1}$ for P3HT [99]. The phase separation must be significantly larger than the exciton diffusion length; a large volume of the film will be effectively dead space. Photons absorbed in these regions have little chance of reaching phase boundary before recombining.

More charges can be collected by arranging interfaces more closely—introducing structure to the phase separation, in other words. This is why nanocrystals are particularly interesting for BHJ films. The nanocrystals can be grown long enough to span the full thickness of the BHJ film, and their shape can be controlled to something more useful than a simple nanorod or dot. Tetrapods [84] and hyperbranched [32] nanocrystals ensure that, no matter how a nanocrystal is oriented, it will provide an electrical connection to the back contact.

Mixing nanocrystals into polymers, however, is no simple task. Nanocrystals and polymers are not necessarily soluble in the same solvent, and the nanocrystal incor-

poration in the polymer will depend dramatically on the attached ligands [3]. So here we investigate photovoltaic BHJ films comprised of CdSe nanoparticles with various ligands and poly (3-hexylthiophene-dyl).

3.2 Fabrication and Treatment

Despite numerous studies showing distinction between CdSe nanoparticles capped with different ligands [42, 47, 65], few photovoltaic studies [2] have been done to determine what effects the various capping ligands have in the final device. The ligands often dominate the electrical performance of the nanocrystals since they can occupy electron surface states that otherwise would act as trap states for charge carriers [42] and can also act as insulators that impede charge transport. The ligands can also be a large driving force in nanocrystal aggregation [38] which can both improve charge transport and modify quantum confinement properties. We demonstrate that solution conditions, as well as ligand, can dramatically affect the blend morphology.

Thermal annealing is commonly employed in device processing and can strongly affect device performance. For polymer-fullerene devices, the enhancement is a result of enhanced phase separation and enhanced polymer crystallinity [67], but for P3HT/CdSe photovoltaics, the mechanism of performance enhancement is less clear. Contrary to previous results, our results suggest that improvements due to annealing are caused by oxygen removal rather than P3HT crystallization.

Under AM1.5G and $100mW/cm^2$, our best devices has yielded short circuit

currents of $6.9\text{mA}/\text{cm}^2$, open circuit voltages of 0.55 V, and fill factors of 0.47 for a power conversion efficiency of 1.8%. This is not a record efficiency for the P3HT/CdSe system, but it is the highest efficiency for CdSe nanodots, demonstrating that clever choice of ligands may prove a viable route to morphology control.

3.3 Experimental

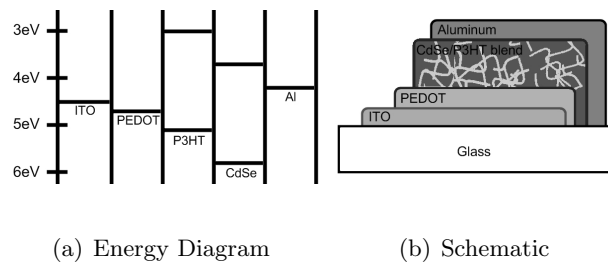


Figure 3.2: Energy diagram and schematic of CdSe/P3HT blended devices.

Figure 3.2(a) shows the energy structure for our devices; they are typical donor-acceptor photovoltaics. Absorption takes place in the nanocrystal/polymer phase, and excitons separate at the NC/polymer interface. By blending the phases, a large surface area is set up to aid this charge separation. Electrons preferentially remain in the NC and are extracted at the Al back electrode, while holes travel in P3HT to the ITO. These devices employ a poly(3,4-ethylenedioxythiophene) poly(styrenesulfonate) (PEDOT:PSS) electron-blocking layer, and holes are blocked from returning to the NC or aluminum contacts by a large offset between the donor HOMO and acceptor LUMO levels and contact fermi levels.

For this study, nanoparticles were synthesized by following the procedure given by Gur *et al* [33]. Trioctylphosphine ligands were replaced with pyridine ligands by stirring the nanocrystals in an excess of pyridine under reflux for twenty-four to forty-eight hours. If desired, a second ligand exchange was then performed using the same procedure with an excess of the replacement ligand. The capping ligands used were pyridine, butylamine, tributylamine, oleic acid, and stearic acid. The nanocrystals were then dispersed in chloroform, and mixed eight parts CdSe with one part of P3HT by weight. These mixtures were then diluted to 33mg/ml of nanoparticles and allowed to stir for at least 48 hours. Devices were prepared on ITO coated glass substrates purchased from Thin Film Devices Inc. The substrates were first cleaned by sonication in detergent at 60°C, deionized water, and ethanol at 40°C. They were then dried in a nitrogen stream. PEDOT:PSS was spin-cast onto the substrates at 3000 rpm and dried under vacuum at 110°C for an hour. Then CdSe nanoparticle/P3HT blend was spin-cast at various spin-speeds and dried for another hour under vacuum at 110°C. Devices were then encapsulated in a nitrogen glove-box before evaporating 50nm thick Al back-contacts.

Most of the nanoparticle/polymer blends were dispersed in pure chloroform, but some devices were made using a blended solvent of chloroform and capping ligand; this was done to control the aggregation of the nanoparticles. The capping ligand makes the nanoparticles soluble, and adding capping ligand to the solvent helps make them more so. [38] The polymer, however, is typically insoluble in the ligand, so a careful balance must be maintained to achieve proper dispersion. Therefore, concentrations of

additional ligand were always kept below five percent.

J-V characteristics were measured with a Keithley 2400 Sourcemeater under AM1.5D ($100mW/cm^2$) simulated by an Oriel model 66902 solar simulator. The light intensity was calibrated using a NREL certified photodiode prior to each measurement. After initial testing, films were annealed for various times, typically at 100°C for thirty minutes, and tested again. Unless otherwise noted, all figures depict devices after post-deposition annealing.

3.4 Results/Discussion

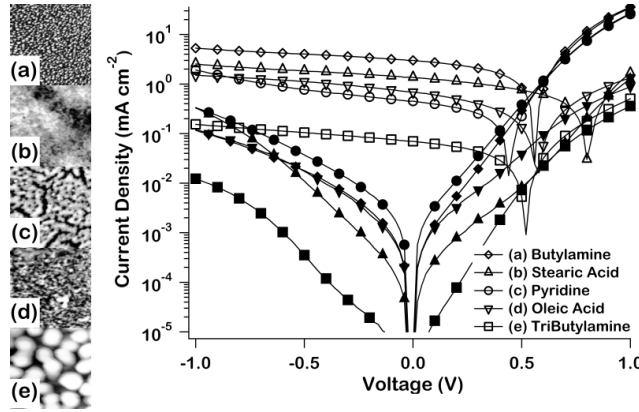


Figure 3.3: AFM images and J-V characteristics of NC/P3HT films identical in preparation except for the NC capping ligand. Ligands used were butylamine (a), stearic acid (b), oleic acid (c), pyridine (d), and tributylamine(e). Each AFM image is $15\mu\text{m}$ square. J-V characteristics of post-production annealed devices. Light currents were recorded under a simulated AM 1.5D spectrum at $100mW/cm^2$

While investigating an alternate ligand exchange procedure, Aldakov et. al. noted that ligand choice affected phase separation [2]. We find the same here, and the level of phase separation dominated the behavior of these devices. Figure 3.3 shows

AFM images and J-V characteristics of films prepared under identical conditions, but made from batches of nanocrystals capped with different capping ligands. The device short-circuit currents are almost completely explicable in terms of phase-separation. Since the diffusion length is at most tens of nanometers, these devices will all be limited by their varying degrees of phase separation. Butylamine provides the best current and smallest morphology features, followed by oleic acid, and tributylamine. Stearic acid devices have 10 micron scale structure, but finer structure on a scale of 500nm exists across the morphology, partially explaining its relatively high performance. The only film not easily explained by phase separation was pyridine; films made with pyridine capped nanocrystals were consistently poor performers, with currents far lower than the phase separation would suggest. In fact, pyridine-capped films were much smoother than other blended films, suggesting a much lower phase separation, which may explain the low currents.

The variation in V_{oc} is a bit tougher to explain. Butylamine, tributylamine, and oleic-acid capped nanocrystals yielded roughly the same V_{oc} , and the low V_{oc} for pyridine-capped nanocrystals is easily explained by shorting, as those films had the highest dark currents. But the anomalously high V_{oc} for the stearic-acid capped nanocrystals is surprising; those films did exhibit low dark currents, although not as low as the tributylamine films. Whether the tributylamine films could achieve the same V_{oc} by virtue of their low dark currents, but simply didn't because the carrier collection was so poor due to high phase separation is an interesting question.

Nanoparticle synthesis has produced many geometries of nanoparticles, such

as nanorods [83], tetrapods [84], and hyperbranched CdSe [32]. Photovoltaics based on these nanoparticles benefit from the varied geometries. CdSe nanorods have better charge transport than simple dots. Tetrapod and hyperbranched nanocrystals may individually traverse the thickness of the film, and, at the very least, will have extensions perpendicular to the substrate, increasing the likelihood of a percolation pathway existing. This enhances performance by giving electrons a path to the photocathode. Top efficiencies for CdSe nanorods, tetrapods, and hyperbranched nanocrystals are 2.6% [83], 2.8% [85] and 2.2% [32], respectively. Our films benefit from a similar morphological advantage due to aggregation; since the aggregate size is often many times larger than the thickness of the film, these nanoparticle aggregates are likely to span the film in exactly the same manner. Some of the least aggregated of our films have average feature sizes larger than the film thickness.

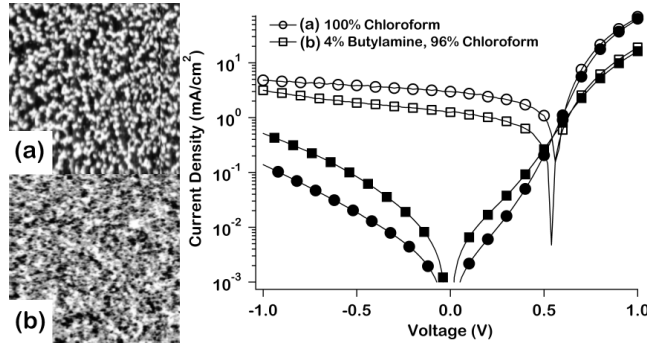


Figure 3.4: AFM images and J-V characteristics of CdSe/P3HT blended films. Films spun from solution containing no ligand(a) were rougher than films spun from solution with ligand(b). Light currents were recorded under a simulated AM 1.5D spectrum at $100mW/cm^2$

Previous works [38] used a tailored solvent to encourage less phase separation; adding capping ligand to the host solvent makes the nanoparticles more soluble at the

expense of the polymer's solubility. This tailored solvent can decrease phase separation in the film. Our attempts to improve the morphology/phase separation in this manner were partially successful. These films became smoother, suggesting less phase separation, and the average feature size decreased, although evidence of aggregation was still present. Despite the improved morphology, photovoltaic performance decreased as the shunt resistance dropped. (See figure 3.4.) This is not likely due to additional ligand trapped in the film, as butylamine's boiling point is 25°C below our processing temperature. More likely the original aggregation level was actually beneficial in this film by providing a percolation pathway in the same way a tetrapod-shaped nanocrystal would have. The pyridine-capped nanocrystals, which exhibited a similar level of aggregation, would likewise exhibit poor currents due to incomplete percolation pathways. A higher loading ratio of CdSe to P3HT may alleviate this problem.

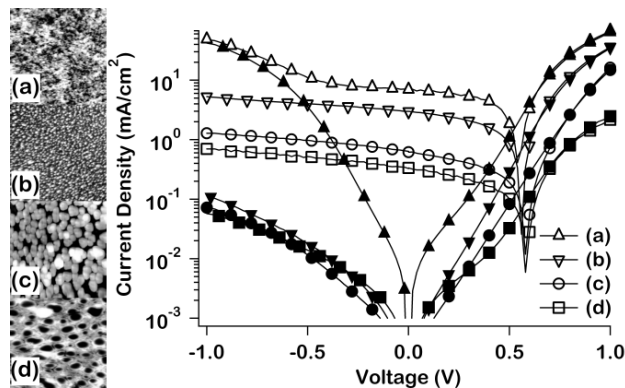


Figure 3.5: J-V characteristics and AFM images of devices made from various batches of butylamine-capped CdSe NC's. Filled shapes depict J-V characteristics in the dark, and empty shapes show J-V characteristics under simulated AM1.5D illumination. Each image is 15 μ m square.

Results can vary significantly between batches of nanoparticles, even with the

same capping-ligand. Each device in figure 3.5 was made from CdSe nanocrystals capped with butylamine. They were prepared under identical conditions, except for sample (a)¹; the difference amongst these films is their parent batch of nanocrystals. A given batch of nanocrystals yielded similar film morphologies, but morphologies between batches varied significantly. This clearly suggests that differences in the nanoparticle solutions are responsible for these differences in morphology. The morphological differences result from differences in ligand exchange efficiency as noted by Sun *et al.* [84]. The cell performance correlates very well with the nanoparticle aggregation again.

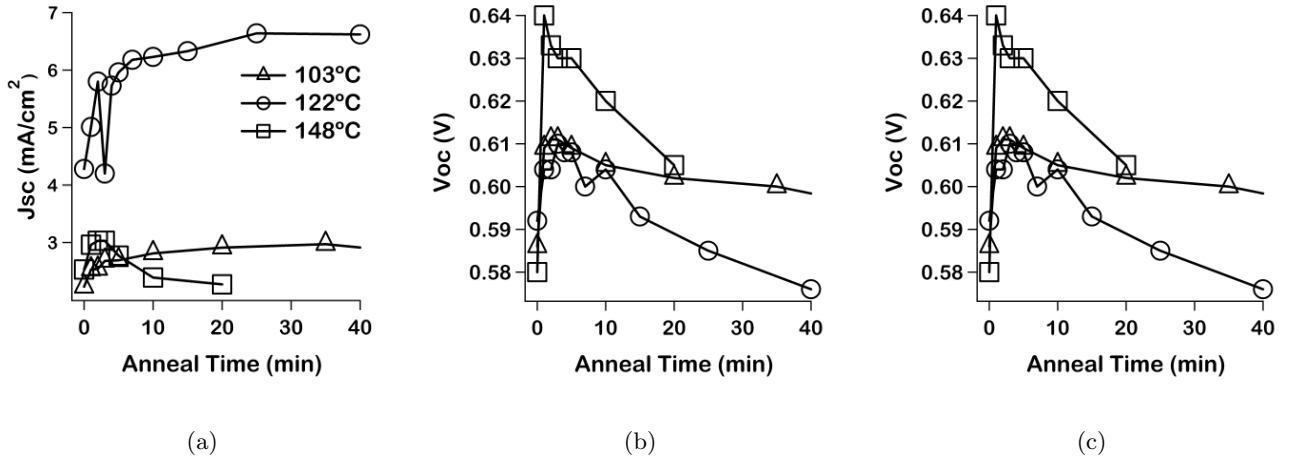


Figure 3.6: Operating parameters are shown for butylamine-capped CdSe/P3HT devices as a function of anneal time. Samples were annealed at 103°C (triangles), 122°C (circles), and 148°C (squares). This annealing was done after back-contact deposition in a nitrogen environment. Device parameters were recorded under AM1.5D at $100\text{mW}/\text{cm}^2$

Figure 3.6 shows a summary of device photovoltaic parameters as a function of annealing for butylamine-capped NP devices. At all temperatures, the devices exhibited a quick spike followed by a modest decline in open-circuit voltage. For the two lower

¹This sample was prepared at a higher loading ratio (27:2) and at a higher concentration (74.5 mg/ml).

temperatures, device parameters increased and stabilized over the course of 30 minutes, but parameters for devices annealed at 148°C degenerated. Most notably, the fill-factor for these devices plummeted to less than 25% within twenty minutes.

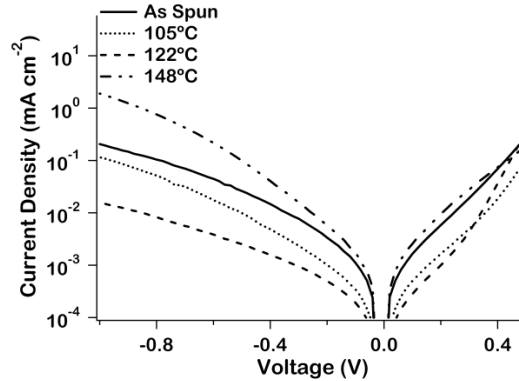


Figure 3.7: J-V characteristics of devices annealed for 20-25 minutes at different temperatures.

Similar studies of annealing thin films of P3HT/PCBM have shown little difference in overall performance between films annealed once only either before or after back-contact deposition [51]. Although our samples are processed at 110°C before back-contact deposition, they are subsequently exposed to oxygen, which quickly diffuses throughout the active layer [52]. Oxygen dissolved in the film would increase conductivity through the P3HT directly to the aluminum back contact, providing a shunt path [1]. Annealing removes this oxygen [56], so the improvement in parameters is expected.

Annealing at 105°C and 122°C serves mostly to remove oxygen from the P3HT, as can be seen in figure 3.7. The lower conductance, indicated by the lower currents in reverse bias, show fewer charge carriers as oxygen leaves the film [1]. However, as the

temperature reaches 148°C, the reverse bias conductance improves. The fill-factor for these films dropped with increasing reverse bias conductance. A similar behavior for ITO/PEDOT-PSS/P3HT/Au devices was observed by Chiguvare [17].

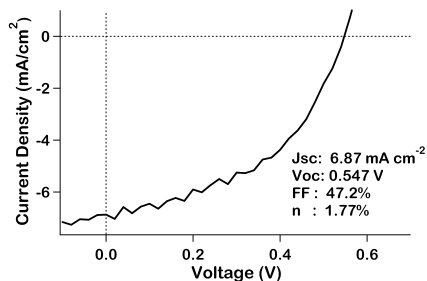


Figure 3.8: JV characteristics of a superior butylamine-capped film. Light currents were recorded under a simulated AM 1.5D spectrum at $100mW/cm^2$. This device displayed 1.8% power efficiency.

Superior butylamine-capped devices were made by changing the loading ratio to twelve parts to one of CdSe nanocrystal to P3HT. These devices were dispersed in chlorobenzene at a concentration of 60mg/ml of CdSe. The resulting films were 130 nm thick. This procedure yielded devices with 0.55 Voc, $6.9mA/cm^2$ Jsc, and a 47% fill-factor. These 1.8% power efficient devices are the best reported to date on CdSe quantum-dot and P3HT blended films. (See figure 3.8) We note that these devices have similar morphologies to optimum devices made from P3HT/CdSe nanorod blends. Furthermore, quantum dot and nanorod devices have very similar power efficiencies when chloroform is used as the solvent [83] which is known to result in less ordered polymer morphology. Quantum dots may have comparable efficiencies to quantum rod devices if a solvent with a higher boiling point was used to improve ordering and therefore hole transport within the polymer.

3.5 Conclusion

We have demonstrated that nanoparticle capping ligands, as well as solution conditions, have a dramatic effect on phase separation in blended nanocrystal/conjugated polymer devices. Optimal morphologies achieve a careful balance between the nanoparticle aggregation needed for good charge transport with phase separation needed for efficient exciton dissociation. Phase separation is heavily influenced by ligand choice, but inefficiencies in the ligand exchange procedure likely contribute to the final film morphology, as evidenced by the varied film morphologies resulting from films produced with different batches of nanocrystals under otherwise identical conditions. A thermal annealing step at around 110°C after isolation from atmospheric conditions is critical to remove oxygen from the P3HT. As has been suggested by other recent work [32], new methods to control the phase separation dynamics in polymer-nanoparticle blends will be important to the future viability of this technology.

Chapter 4

Inorganic Thin-Film

4.1 Sintered nanocrystal films

Nanocrystals are an interesting compromise between organic donor-acceptor photovoltaics and smooth inorganic thin-film photovoltaics. Nanocrystal films can be formed without sintering [53], and still maintain their quantum-confined absorption profile, yet exhibit electrical characteristics more akin to photovoltaics formed by smooth, continuous films. Charge carriers travel by hopping, and mobilities are low [31].

Nanocrystals share so many properties with organic films that the original report on photovoltaic films from sintered nanocrystals concluded that the films were donor-acceptor systems [33]. So our goal in this research was two-fold: to determine the underlying physics of our sintered nanocrystalline films and to optimize processing parameters for a high efficiency device.

In this study, we examine the optical and electrical properties of sintered pho-

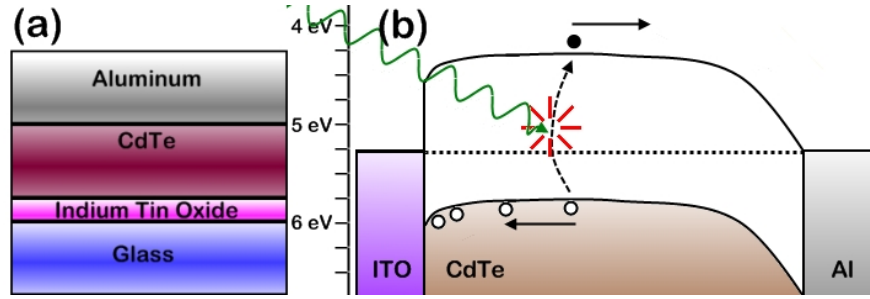


Figure 4.1: Device structure (a) and energy diagram (b).

tovoltaic CdTe films. Films are fabricated by spin-casting CdTe nanorods onto clean ITO coated substrates. The resulting film is coated with cadmium chloride (CdCl_2), then sintered at 400°C . The films are then rinsed in hot water to remove any remaining cadmium chloride before they are capped with evaporated aluminum. Figure 4.1 shows the device structure and expected energy structure for sintered CdTe films. Under illumination, electrons are excited and collected at the aluminum contact, while holes are collected through the ITO.

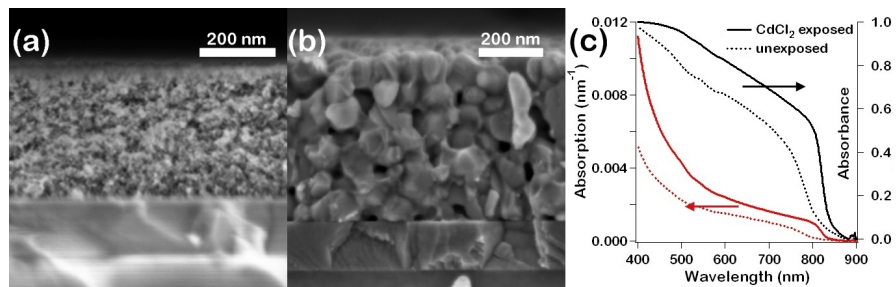


Figure 4.2: SEM images of CdTe nanorods before (a) and after exposure to CdCl_2 vapors at 400°C , and optical absorption increase (c). In the Beer-Lambert law ($I = I_0 e^{-\alpha l}$), α is the absorption and the fraction I/I_0 is the absorbance, which is specific to a given optical path-length l . The calculated absorbance is for the same thickness as our champion device after accounting for reflection from the back contact.

Figure 4.2 is an SEM micrograph of sintered nanocrystal films constructed

with (a) and without (b) exposure to CdCl_2 vapor. As others [49, 58, 59] have seen, sintering with CdCl_2 vapors resulted in grain growth. Grain growth would improve transport through our films since grain boundaries act as electrical barriers that carriers must cross [14]. The final grain size is about an order smaller than those seen with other deposition technologies such as CSS or PVD, but this is unsurprising as those technologies deposit CdTe with micron-scale grains before CdCl_2 treatment [59].

In addition to grain growth, an overall increase in optical absorption was observed, as illustrated in figure 4.2c. Although many other studies note increased absorption near the band edge [49, 58], none to our knowledge have measured absorption in CdTe throughout the visible spectrum. If the absorption change in our films is due primarily to the morphological change from nano-scale grains to micro-scale grains, this would have no implications for CdTe films deposited by other technologies since those films have micro-scale grains before CdCl_2 treatment. If, however, the absorption improvement is due to a change of trap distribution, or due to an increase of average monocrystalline domain size, CdS/CdTe photovoltaics should also have enhanced absorption with CdCl_2 treatment. This would improve device efficiency across the visible spectrum with slightly more improvement in the red. Although CdTe can absorb all light in its bandwidth within a micron or so, full absorption does not occur on the scale of the minority carrier diffusion length [90], and electrons absorbed far from the CdS/CdTe interface are more likely to recombine in p-type CdTe than those collected close to the interface. Increasing the optical density of CdTe should increase collection of these carriers by shortening the distance they must travel. This sort of EQE enhancement has

been observed by Moutinho *et al.* [71], but whether those results are due to enhanced optical absorption would require careful numerical analysis.

Schulmeyer *et al.* [75] found that over-treating CdTe CSS films resulted in device shunting; our films also shunt when overtreated. SEM images reveal pores distributed throughout the sintered film, so pinholes are an obvious mechanism for shunting(see figure 4.2b), although long treatment times should result in larger grains [27], so it isn't clear whether short treatment or long treatment would result in more pinholes. Images of overtreated film temperature under bias reveal no large, localized temperature variations, so if pinholes form, they would need to be plentiful, and should have been detected under AFM. Therefore we do not believe shunting to be caused by pinholes.

The shunting could also be due to a conducting layer of film that forms along grain boundaries during treatment, however. Surface oxides are found in CdTe films after CdCl₂ treatment under even the most careful conditions [63, 75]. Our CdCl₂ activations step is carried out in air, as is typical for CdTe films, so such an oxide layer will inevitably form. The only question is the chemistry, morphology, and effect of this oxide layer.

Several studies [26, 44, 57, 63] have been done to find the effects of the CdCl₂ treatment in the presence and absence of oxygen. Niles *et al.* [63] used X-ray photoelectron spectroscopy to examine the surface of CdCl₂ activated CdTe films. In the presence and absence of oxygen, they found similar concentrations of surface oxygen, and concluded that CdO had formed. CdO is a transparent conductor [34]. Given the large number of voids in our films, if such a conducting layer can form, it's surprising

working devices could be produced at all. Even in films without voids, diffusion along grain boundaries would provide a means for a conducting oxide to form between the anode and cathode, but the process would be much faster in our porous ultra-thin films, as is evidenced by our five-minute sintering time.

Cadmium metal could also be responsible for this shunting; although nanocrystals are highly crystalline, their stoichiometries can vary significantly from monocrystalline values because of the large number of surface ions [39]. Excess cadmium at the surface may migrate as an impurity to grain boundaries and provide another means to short devices; the resistivity of cadmium is only four times larger than copper. The mechanism by which these films short is of supreme interest to our group and is currently under investigation.

CdTe can be doped either n-type or p-type [95], and its doping sign can switch during processing [7], so the sign of the majority carriers is not obvious. CdS/CdTe devices employ p-type CdTe, but n-type CdTe can certainly be deposited [7]. The dopants present, however, suggest that our films are p-type. Studies of ligand exchange efficiencies [3,13,46,93] consistently reveal exchange efficiencies of 90% or less. Assuming only 30% ligand coverage of surface ions as estimated by Kuno *et al* [46], and given that roughly one in five ions is a surface ion given a 6nm radius [82], the sintered nanocrystal film will still have a phosphorous content on the order of 10^{20}cm^{-3} . Phosphorous is an effective p-dopant for CdTe [35,95], but high levels of p-dopants are compensated, and the highest p-dopant level achieved for CdTe is currently $2.8 \cdot 10^{17} \text{cm}^{-3}$, achieved with a P content of $2 \cdot 10^{19} \text{cm}^{-3}$ [35].

X-ray fluorescence measurements of our films revealed an obvious phosphorous peak, but we have not determined quantitatively the amount of phosphorous in our films. We believe this phosphorous is from unexchanged TOPO ligands used to initially cap the nanocrystals. Other contaminants could also exist in our film that can also act as dopants; carbon, and oxygen from burnt ligands, nitrogen, and every native defect possible could exist in concentrations similar to our phosphorous concentration. However, phosphorous ions on tellurium sites are particularly effective p-dopants [95], and recrystallization should reduce native defects by orders of magnitude(see figure 4.2a and b). So we assume that our CdTe films are p-type, with many more phosphorous ions than holes.

Having formed some picture of the morphology, composition and absorbance of these devices, it is important to determine what physics generated the photoaction. The obvious mechanism is a schottky-barrier formed at the CdTe/Al interface: schottky because there is a single semiconductor present, and CdTe/Al interface because the band-bending should be largest at that interface given the work-functions of ITO and Al. It is possible to imagine a p-n junction through some spacially dependent doping-profile formed during the sintering process; the introduction of indium, a CdTe n-dopant [95], through the front contact could result in a p-n junction in our films. Indium will diffuse through CdTe at our processing temperatures [26], but this would result in the aluminum back-contact extracting holes, as the n-type region of CdTe would contact the ITO. So this mechanism can be ruled out. CdTe films are exposed to chlorine, a deep n-type dopant [95], but the distribution of chlorine after sintering is not spacially

dependent [26], and the primary expected result of adding chlorine to a CdTe film is to improve p-doping through co-doping [95]. Aluminum is also a CdTe n-dopant, so the proper polarity doping profile could be obtained by diffusion of the Al from the back contact into the film. Since we were able to construct similar devices using Al or Ca/Al contacts, this mechanism isn't likely. Moreover, we do not use an annealing step after back-contact deposition. Any such n-doped region should be confined to a very small volume near the back contact, in which case it would be difficult to distinguish from a Schottky diode.

Even a donor-acceptor mechanism can be envisioned by some n-type surface oxide coating the grains and providing the acceptor phase. Donor-acceptor photovoltaics rely upon an interpenetrating network of hole and electron transporters which conduct their charge carriers to their respective electrodes [89]. These interpenetrating networks must be carefully engineered to match the exciton diffusion length so that charge carriers can split into their respective phases; typically, these carriers are limited by low mobilities. CdTe has high mobilities for electrons and holes alike [91], and would readily conduct both charge carriers. CdO is an n-type "semiconductor", but with carrier concentrations of 10^{20}cm^{-3} from intrinsic defects [34], its behavior is metallic, and its formation would be undesirable according to our observations.

Figure 4.3 shows current-voltage characteristics for a champion device (a and b) and our measured external quantum efficiency(c), corrected to be self-consistent with our measured short circuit current. I-V characteristics were measured under simulated AM1.5G 100 mW cm^{-2} conditions. Our resulting power efficiency is 5.3%, and we

predict 5.0% efficiency after correcting for spectral mismatch. Also shown in figure 4.3c is absorptance calculated for this thickness of CdTe using a different sample and the Beer-Lambert law, $I = I_0 e^{-\alpha l}$. Near the band-edge, to within experimental error, the internal quantum efficiency approaches unity. This particular CdTe device had a thickness of 360nm—about 10% of the material used in more established CdTe deposition techniques, and without depositing any CdS.

I-V curves displayed two characteristics: current roll-over above V_{oc} and a dark current several orders of magnitude lower than the light current. The extremely low dark currents suggest that the films had low carrier concentrations in the dark. Chakrabarti *et. al.* also showed that tunneling barriers at grain boundaries are larger and wider in the dark than in the light, further impeding current [14]. The roll-over at forward bias indicates non-ohmic contact between the ITO and CdTe. Shorter wavelengths are collected with slightly less efficiency; the charges excited close to the ITO are less likely to reach an electrode. The champion device in figure 4.3 had a thickness of 360nm; this is on the order of the minority carrier diffusion length [90], so a free electron collected near the ITO would have some hope of reaching the photoanode.

Internal quantum efficiency measurements provide a means to assess the position of our rectifying barrier. Since the optical density is higher at blue wavelengths than red, on the average, blue light will be absorbed closer to the ITO than red light. External quantum efficiency measurements over a variety of thicknesses reveal that, as devices become thicker, their current under blue illumination decreases. (See figure 4.4.) This suggests that our back-contact is responsible for the photo-action; minority carriers

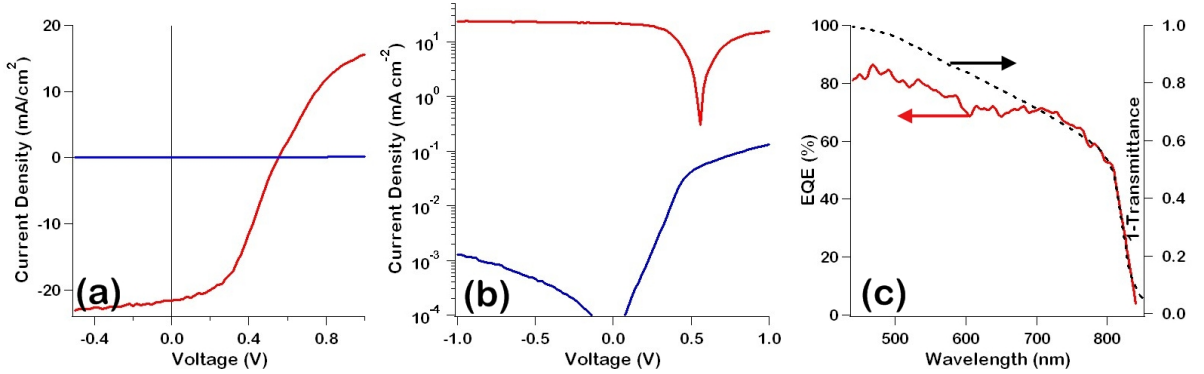


Figure 4.3: I-V characteristics on linear (a) and semilog (b) scales, and self-consistent external-quantum efficiency and calculated absorptance curves(c). Light characteristics were measured under simulated AM1.5G 100 mW cm^{-2} conditions. Photovoltaic parameters are as follows: J_{sc} 21.6 mA cm^{-2} , V_{oc} 540 mV, fill-factor 45.5%, PCE 5.3%. Adjusted for spectral mismatch, short-circuit density would be 20.4 mA cm^{-2} , and PCE would be 5.0%.

excited far from their electrode will be more likely to recombine. The external quantum efficiency curves in figure 4.4 are inconsistent with figure 4.3(c), but some absorptance variation in this material is expected, as CdTe forms oxides that are highly transmissive at visible wavelengths [34], so varying concentrations of oxygen in the film would result in lower optical density.

$J_o = A^{**}T^2 e^{-q\phi_{beff}/k_B T}$ describes the expected current from thermionic emission [69], where J_o is the reverse saturation current density, A^{**} is the effective Richardson constant, and ϕ_{beff} is the effective barrier height. A bit of algebra yields

$$\ln\left(\frac{J_o}{T^2}\right) = \ln(A^{**}) + \frac{-q\phi_{beff}}{k_B T}$$

By plotting $\ln(\frac{J_o}{T^2})$ against $\frac{1}{T}$, ϕ_{beff} can be determined. Figure 4.5 shows the temperature dependence of our devices. The temperature dependence suggests thermionic emission with a barrier height of $800 \text{ meV} \pm 50$, well-matched to our expected value [86].

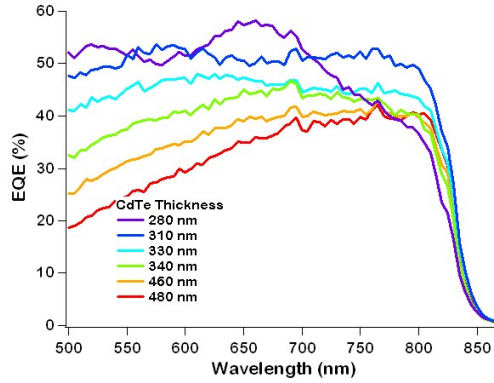


Figure 4.4: External quantum efficiencies for various thicknesses of CdTe layer. Recombination in the blue indicates back-contact band bending.

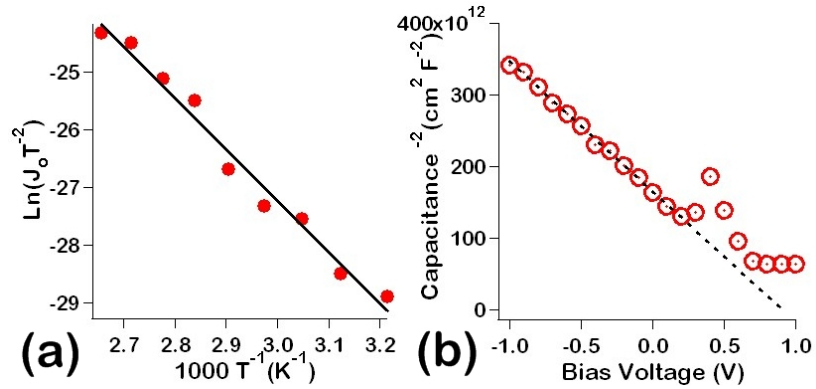


Figure 4.5: Arrhenius plot (a) and capacitance-voltage measurements (b) of photovoltaic CdTe films. Both of these measurements suggest Schottky barrier formation.

Additionally, capacitance-voltage measurements suggest a Schottky barrier.

As the reverse bias voltage extends the depletion region, capacitance drops, described by $C = A(\epsilon\epsilon_0 N_d/2)^{1/2}(V - \phi_{beff} - \frac{k_B T}{q})^{-1/2}$ [10]. A is the device area, V is the reverse-bias voltage. $\frac{k_B T}{q}$ can be ignored at room temperature as it is much smaller than V_{bi} .

A good linear fit can be made to

$$\frac{A^2}{C^2} = \frac{\epsilon\epsilon_0 N_d}{2}(V - \phi_{beff})$$

Deep traps, surface states, and non-ohmic contacts make C-V profiling quantitatively challenging on CdTe [21, 61], but our measured profile does match the expected linear dependence of C^{-2} on V in reverse bias and yields quantitatively reasonable numbers (around $7 \cdot 10^{16} \text{cm}^{-3}$), again suggesting a Schottky barrier.

4.2 Conclusion

To summarize, we have fabricated photovoltaic devices from CdTe nanocrystals with only a single layer of semiconductor. These films act as schottky diodes with non-ohmic contacts on heavily compensated p-type CdTe. These films are only 360nm thick, but have short-circuit current densities comparable to much thicker CdTe films, and have demonstrated a power conversion efficiency of over 5%. By studying ultra-thin layers of CdTe, we have observed increased optical absorption throughout the visible spectrum after treatment with CdCl₂ vapor, and have presented evidence for an undesirable film—either CdO or Cd—that forms simultaneously with CdCl₂ treatment. This increased absorption could help explain the current improvements to CdS/CdTe films, as the optical absorption length in CdTe is larger than the minority carrier diffusion length.

Chapter 5

Conclusion

We have shown, either through simulation or actual experimental devices, three means to achieve solar power via very low cost techniques. For the case of luminescent solar concentrators, highly photoluminescent materials with emission in the near-IR must be used. Assuming no significant transmissive losses other than those due to reabsorption, we have shown that LSC should provide an affordable route to solar energy given desirable but realistic material properties.

For blended CdSe nanocrystal/P3HT thin films, we have shown that the morphology depends mostly upon material preparation and device processing, and that the phase separation is dominated by the nanocrystal ligand population, including unexchanged ligands from the initial TOPO capping. Controlling this morphology is expected to be quite challenging, and, given the limits for BHJ solar cells due to the exciton diffusion length, required film thickness for good spectral absorption, and typical large-scale phase separation, this technology will be difficult to develop into a viable

commercial option using CdSe nanodots. Branched CdSe nanocrystals or other means of ensuring good percolation pathways throughout the film bulk should produce much faster progress.

For the case of sintered CdTe nanocrystals, we have shown that the finished film behavior is that of a traditional inorganic Schottky diode, not a donor-acceptor film as previously believed. We have shown improved optical density accompanying the grain growth that occurs with high temperature exposure to CdCl₂, providing an additional mechanism for improvement in our films and the established CdS/CdTe solar cell films. We've also shown evidence for a conducting layer formed at the grain boundaries, probably due to excess cadmium. Power efficiencies above 5% have been demonstrated using only a single layer of sintered nanocrystals.

Appendix A

Optical techniques

A.1 Monochromator Calibration

This section is included for practical reasons. The monochromator is a simple instrument, but it isn't difficult to misalign a slit or ignore a secondary peak and make flawed measurements. For this reason, it's important to check the spectrum and intensity leaving the monochromator before making a measurement.

Figure A.1 shows a basic monochromator. White light shines in through the slit on the left, reflects off a mirror and onto a diffraction grating. The diffraction grating spreads the beam into its various components, which reflect off a second mirror and out through a second slit.

Ideally, the outgoing light will be a delta-function in wavelength—infinite intensity and infinitely narrow. Obviously it won't be. For a real setup, compromises must be made. As the slits become narrower, the spectrum allowed to exit the monochro-

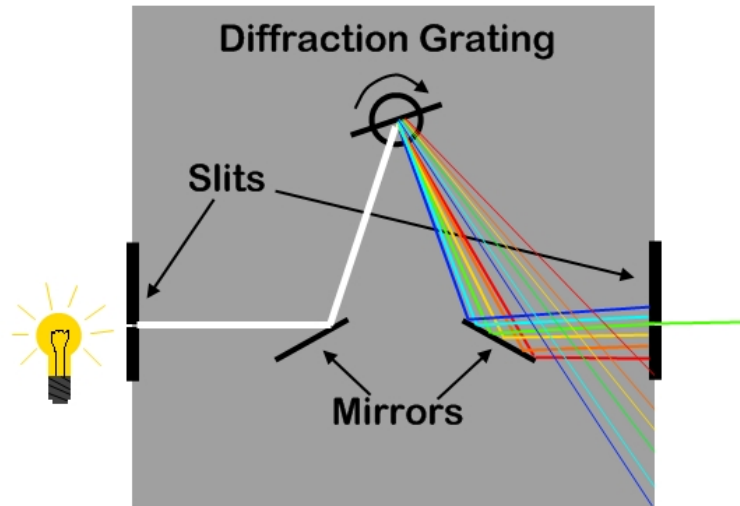


Figure A.1: A simplified monochromator schematic. Most real monochromators include additional mirrors to increase the light path length, and filters to eliminate secondary peaks, shown as thin lines.

mator will become narrower. But, simultaneously, less light is being admitted into the monochromator, so the resulting spectrum becomes less intense, and the resulting signal-to-noise ratio will decrease. Larger slits can be used to boost the intensity, but the spectrum exiting the monochromator becomes broader.

For this monochromator, there is no mechanism to ensure that the desired wavelength is actually being emitted at the other end. The monochromator receives a request from a computer to emit a certain wavelength of light and rotates the diffraction grating to whichever angle should result in that wavelength. But the emitted wavelength depends not only on the position of the diffraction grating, but the position of the slits and the alignment of the incoming light. The calibration must be done by the user, and there are essentially two methods.

The first method is to connect the monochromator to the spectrometer, request a specific wavelength, and then adjust the slits until the resulting spectrum has as much intensity as possible at the appropriate wavelength. For a good monochromator, the incoming slit should first be adjusted to maximize the intensity, then the outgoing slit can be adjusted to select the appropriate wavelength. However, if the requested and emitted wavelengths are different enough, the slit position for peak intensity at the desired wavelength may not coincide with the initial wavelength's peak intensity. So the best technique the author has found to maximize the monochromator intensity at a specific wavelength is simply to fiddle with the slit positions while watching the output spectrum.

The first method has the advantage of being intuitive, but the emitted light may not be at the peak intensity. This second method corrects this. Instead of forcing the monochromator to emit a spectrum at the requested wavelength, we can adjust the data to match the monochromator. To do this, the user first measures the spectrum using the spectrometer, as before, and adjusts the slit positions. However, instead of setting the emitted spectrum to the requested wavelength, this time the user adjusts the slits only to maximize intensity with no regard for wavelength. The resulting spectrum will then have some offset between the requested and resulting wavelength. This offset should be much smaller than the wavelength, and approximately constant throughout the range of measurement. The offset can then either be added to the wavelength request in the software or manually subtracted from the raw data by the user. This technique allows the monochromator to emit the highest intensity with almost no disadvantage.

Care must be taken to filter out secondary peaks. Longpass or bandpass optical filters should be used appropriately to ensure that only primary peaks are transmitted. Since we are interested only in visible and infrared light, no more than two longpass filters should be necessary. With proper insertion of one longpass with a 700nm cutoff, and a 1400nm cutoff longpass, secondary peaks can be eliminated out to 2800nm, which have less than $\frac{1}{2}eV$ of energy, and are not useful photons for most solar cells.

A.2 Measuring External Quantum Efficiency

External quantum efficiency (EQE) is the fraction of electrons collected per incident photon, or

$$EQE \equiv \frac{\#electrons}{photon}(\lambda)$$

The EQE will merely follow the contour of the absorption spectrum if absorption is poor or if collection is limited to a narrow depletion region at the front of the device. For good transport and good optical absorption, the EQE spectrum should be more or less flat, only following absorption at the band edge.

Measuring EQE is a two step process. Rather than integrating the monochromator spectrum at every datapoint to count the total number of photons, we will measure a current and compare it to current read from a reference solar cell whose EQE is known. At a given wavelength, current will be given by

$$J_{exp}(\lambda) = \Phi(\lambda) \cdot EQE_{exp}$$

We could write a similar equation for our reference cell. $\Phi(\lambda)$ is the incident

photon flux density from the light source. If we use the same source intensity for the two cells, we can write

$$\frac{EQE_{exp}(\lambda)}{J_{exp}}(\lambda) = \frac{EQE_{ref}(\lambda)}{J_{ref}}$$

The experimental EQE can readily be found from this.

This measurement is not foolproof, however. Because the excitation spectrum is so narrow, the photocurrents measured are often quite small—perhaps a few microamps. Source-meters sometimes have trouble finding a true zero-bias, and often some DC current can be observed at supposed zero-bias. If a device has a small R_{shunt} , this zero-bias current can be of the same order as the photocurrent excited by the monochromator. To extract a meaningful calculation of EQE, one should subtract this zero-bias current. The value of this current is best found by examining a region of $J_{exp}(\lambda)$ where there is essentially no light intensity.

A.2.1 Counting Photons

Frequently the “self-consistent” EQE is reported. There *should* be little difference between the initially measured and self-consistent EQE, but calculating currents from an EQE spectrum is a useful tool for checking light intensities, calculating maximum possible currents, and computer simulation. So the calculation is included here. Taking equation A.2 one step further,

$$J_{sc} = C \cdot \int EQE(\lambda) \cdot \Phi(\lambda) \cdot qd\lambda$$

C is a constant representing either an error between the measured J_{sc} and

EQE , or some device degradation that has occurred between the two measurements, and q is the fundamental charge. C can then be used to ensure that reported J_{sc} and EQE are self-consistent.

This calculation is much more versatile, however, because it is very simple. Using a known EQE spectrum, one can calculate the current expected from a true AM1.5G spectrum to predict the mismatch between the simulated spectrum and accepted standard. Alternatively, this can be used to ensure that simulated light intensity is similar to AM1.5G for initial light-source calibration.

A.3 Measuring Fluorescence Quantum Yield

The most dominant photon loss mechanism for the materials used in our luminescent solar concentrators (LSC's) was a failure of the absorber to fluoresce. An excited electron is not guaranteed to emit a photon; non-radiative paths are available to the electron to reach the valence band again [45]. If fluorescence is the fastest available path, fluorescence will dominate and the fluorescence quantum yield (ϕ_f) will be near unity. If a non-radiative path is faster, then the material will fluoresce poorly, and the ϕ_f will be near zero. Many "fluorescent" absorbers are much closer the second extreme than the first, and many good fluorescent materials have ϕ_f significantly less than unity.

Measuring ϕ_f is non-trivial. To measure ϕ_f directly, one must account for every photon. To do this precisely is a science in itself. However, if one is willing to simply compare the intensity of emission to a standard, and assume that the standard's

fluorescence is equal to established values, the measurement can be greatly simplified. The simplified measurement only requires a spectrometer and an excitation source.

So, to measure ϕ_f , we need to measure fluorescence from a standard and our material of interest. ϕ_f is defined as

$$\phi_f \equiv \frac{\textit{photons emitted}}{\textit{photons absorbed}}$$

The absorber of interest (and standard) should be dissolved in a solution dilute enough that the maximum absorptance over the optical path length is around 5%. Typically this measurement is done in an optical cuvette, so the path length is 1 cm. If the absorber is too optically dense, significant numbers of emitted photons will be reabsorbed, the emission curve will redshifted, and the resulting ϕ_f value will be reduced. Absorptance (A) is derived from Beer-Lambert as $A = 1 - \exp \alpha Ml$. The number of absorbed photons will be proportional to

$$\textit{photons}_{abs} \propto \int A(\lambda) \cdot I_{ex}(\lambda) d\lambda$$

where I_{ex} represents excitation source intensity. Similarly, photons emitted will be proportional to

$$\textit{photons}_{em} \propto \int \frac{I_{em}(\lambda)}{n_{slvnt}^2} d\lambda$$

n_{slvnt}^2 enters this relation because light intensity will be reduced by $\frac{1}{n^2}$ when a source originating in a medium is observed from outside that medium [48]. This should be a small correction, as indices for most solvents are somewhere between 1.4–1.5.

Since some proportionality constant of geometric origin remains unknown, the ϕ_f will be measured relative to our known fluorescence standard, ϕ_r . Absorbance and emission spectra must therefore also be measured for this reference material. This gives

$$\phi_f = \frac{\left(\frac{n^2 \cdot \int I_{em}(\lambda) d\lambda}{\int A(\lambda) \cdot I_{ex}(\lambda) d\lambda} \right)}{\left(\frac{n_R^2 \cdot \int I_{Rem}(\lambda) d\lambda}{\int A_R(\lambda) \cdot I_{ex}(\lambda) d\lambda} \right)} \cdot \phi_r$$

This measurement is a bit crude, as the low optical density can be a challenge to control and the ϕ_f can only be as accurate as the standard. But this technique is *much* easier than the alternative of counting photons directly, and can thus be done much more quickly and without specialized equipment.

Appendix B

Monte-Carlo Simulation

B.1 Random Generation of a Spectrum

Here, “random generation” is selecting a single wavelength from a pre-defined distribution of wavelengths—the solar spectrum, for example. This is readily accomplished with two random numbers. The example below is coded in C; *spectrum* is an array containing emission coefficients. This array has been normalized such that its largest value is one. *wavelement* is the candidate wavelength.

```
#define DRAN( X ) (((double)rand()/(((double)RAND_MAX+1)/(X)))
/*DRAN returns a double in the range [0:X)*/

...
//(in Main)
do {wavelement=(int)DRAN(wavrange);}
while (DRAN(1)>spectrum[wavelement]);
/*actual wavelength will be wavelement + the wavelength of
the 0th element in spectrum*/
```

This simple procedure will reproduce the spectral outline of the array provided it is repeated sufficiently. This is the most straightforward method for generating a given spectrum, but it will be near-optimal for broad spectra without high spikes.

B.2 Generating random points on a unit sphere

Choosing a random direction for emission is a spherically symmetric problem, so the natural coordinate system will be spherical. Instead of envisioning randomly distributed vectors, it may be more intuitive to picture dots randomly placed on a unit sphere. Some care must be taken when randomly selecting θ . The surface area of a unit sphere, or solid angle, is given by

$$\int \sin(\theta)d\theta \int d\phi = (\cos(\theta_1) - \cos(\theta_2))\Delta\phi$$

To be an even distribution on the unit sphere, the dot-free solid angle empty around each dot should have no spacial dependence. If random directions are chosen using a flat distribution in θ , dots will be very close together near the z-axis and far apart near the $\theta = 90^\circ$ plane. ($\cos(\theta_1) - \cos(\theta_2)$ be very small for small θ , so little area will result, meaning little area between dots.) Equal steps in solid angle require equal steps in $\cos(\theta)$, so a random number chosen by the computer should be assigned as $\cos(\theta)$. A flat distribution in ϕ will produce the correct spacial distribution of points.

Bibliography

- [1] M.S.A. Abdou, F.P. Orfino, Y. Son, and S. Holdcroft. Interaction of oxygen and conjugated polymers: charge transfer complex formation with poly(3-alkylthiophenes). *J. Am. Chem. Soc.*, 119:4518–4524, 1997.
- [2] D. Aldakov, F. Chandezon, R.D. Bettignies, M. Firon, P. Reiss, and A. Pron. Hybrid organic-inorganic nanomaterials: ligand effects. *Eur. Phys. J. Appl. Phys.*, 36:261–265, 2006.
- [3] D. Aldakov, F. Chandezon, R. De Bettignies, M. Firon, P. Reiss, and A. Pron. Hybrid organic-inorganic nanomaterials: ligand effects. *Eur. Phys. J. Appl. Phys.*, 36:261–265, 2007.
- [4] I.E. Anderson, A.J. Breeze, J.D. Olson, L. Yang, Y. Sahoo, and S.A. Carter. All-inorganic spin-cast nanoparticle solar cells with nonselective electrodes. *Appl. Phys. Lett.*, 94:063101, 2009.
- [5] A.M. Ballantyne, J.S. Wilson, J. Nelson, D.D.C. Bradley, J.R. Durrant, M. Heeney, W. Duffy, and I. McCulloch. The exciton binding energy in luminescent conjugated polymers. In Kafafi and Lane [41], page 633408.
- [6] B.M. Basol. Electrodeposited cdte and hgcdte solar cells. *Solar Cells*, 23:69–88, 1988.
- [7] B.M. Basol, S.S. Ou, and O.M. Stafsudd. Type conversion, contacts, and surface effects in electroplated cdte films. *J. Appl. Phys.*, 58:3809, 1985.
- [8] B.M. Basol and O.M. Stafsudd. Determination of trap parameters in electrodeposited cdte by schottky barrier capacitance measurements. *Thin Solid Films*, 78:217–222, 1981.
- [9] B.M. Basol and O.M. Stafsudd. Determination of trap parameters in electrodeposited cdte by schottky barrier capacitance measurements. *Thin Solid Films*, 78:217–222, 1981.

- [10] P. Blood and J.W. Orton. *The Electrical Characterization of Semiconductors: Majority Carriers and Electron States*, pages 222,231,331–335. Academic Press, 1992.
- [11] S. Bonilla and E.A. Dalchiele. Electrochemical deposition and characterization of cdte polycrystalline thin films. *Thin Solid Films*, 204:397–403, April 1991.
- [12] J.L. Brédas, J. Cornila, and A.J. Heeger. The exciton binding energy in luminescent conjugated polymers. *Advanced Materials*, 8(5):447–452, 1996.
- [13] A. Caragheorghopol and V. Chechik. Mechanistic aspects of ligand exchange on au nanoparticles. *Phys. Chem. Chem. Phys.*, 10:5029–5041, 2008.
- [14] R. Chakrabarti, J. Dutta, A.B. Maity, S. Chaudhuri, and A.K. Pal. Photoconductivity of cdte films. *Thin Solid Films*, 288:32–35, 1996.
- [15] S.V. Chasteen. *Exciton dynamics in conjugated polymer photovoltaics: steady-state and time-resolved optical spectroscopy*. University of California at Santa Cruz, December 2005.
- [16] Y. Chiba, A. Islam, Y. Watanabe, R. Komiya, N. Koide, and L. Han. Dye-sensitized solar cells with conversion efficiency of 11.1%. *Japanese Journal of Applied Physics*, 45(25):L638–L640, 2006.
- [17] Z. Chiguvare. *Electrical and optical characterisation of bulk heterojunction polymer-fullerene solar cells*. Oldenburg University, Oldenburg, Germany, February 2005.
- [18] J.P. Clifford, K.W. Johnston, L. Levina, and E.H. Sargent. Schottky barriers to colloidal quantum dot films. *Appl. Phys. Lett.*, 91:253117, 2007.
- [19] A.S. Davydov. *Theory of Molecular Excitons*. Plenum Press, ?, 1971. ?
- [20] D.L. Dexter. Interpretation of urbach’s rule. *Physical Review Letters*, 19(24):1383–1385, October 1967.
- [21] I.M. Dharmadasa, C.J. Blomfield, C.G. Scott, R. Coratger, F. Ajustron, and J. Beauvillain. Metal/n-cdte interfaces: a study of electrical contacts by deep level transient spectroscopy and ballistic electron emission microscopy. *Solid-State Electron.*, 42(4):595–604, 1998.
- [22] I.M. Dharmadasa, C.J. Blomfield, C.G. Scott, R. Coratger, F. Ajustron, and J. Beauvillain. Metal/n-cdte interfaces: a study of electrical contacts by deep level transient spectroscopy and ballistic electron emission microscopy. *Solid State Electron.*, 42(4):595–604, 1998.
- [23] M.H. Du, H. Takenaka, and D.J. Singh. Carrier compensation in semi-insulating cdte: First-principles calculations. *Phys. Rev. B*, 77(1):094122, 2008.

- [24] D.F. Eaton. Reference materials for fluorescence measurement. *Pure and Applied Chemistry*, 60(7):1107–1114, 1988.
- [25] R.J. Ellingson, M.C. Beard, J.C. Johnson, P. Yu, O.I. Micic, A.J. Nozik, A. Shabaev, and A.L. Efros. Highly efficient multiple exciton generation in colloidal pbse and pbs quantum dots. *Nano Lett.*, 5(5):865–871, 2005.
- [26] M. Emziane, K. Durose, N. Romeo, A. Bosio, and D.P. Halliday. Effect of cdcl_2 activation on the impurity distribution in cdte/cds solar cell structures. *Thin Solid Films*, 480-481:377–381, 2005.
- [27] Z.Z. Fang and H. Wang. Densification and grain growth during sintering of nano-sized particles. *Int. Mater. Rev.*, 53(6):326–352, 2008.
- [28] M. Fiederle, C. Eiche, M. Salk, R. Schwarz, K.W. Benz, W. Stadler, D.M. Hofmann, and B.K. Meyer. Modified compensation model of cdte. *Journal of Applied Physics*, 84(12):6689–6692, December 1998.
- [29] A. Franceschetti, H. Fu, L.W. Wang, and A. Zunger. Many-body pseudopotential theory of excitons in inp and cdse quantum dots. *Physical Review B*, 60(3):1819–1830, 1999.
- [30] J.I. Gersten and F.W. Smith. *The Physics and Chemistry of Materials*, page 388. Wiley-Interscience, 2001.
- [31] D.S. Ginger and N.C. Greenham. Charge injection and transport in films of cdse nanocrystals. *J. Appl. Phys.*, 87(3):1361–1368, 2000.
- [32] I. Gur, N.A. Fromer, C. Chen, A.G. Kanaras, and A.P. Alivisatos. Hybrid solar cells with prescribed nanoscale morphologies based on hyperbranched semiconductor nanocrystals. *Nano. Lett.*, 7:409–414, 2007.
- [33] I. Gur, N.A. Fromer, M.L. Geier, and A.P. Alivisatos. Air-stable all-inorganic nanocrystal solar cells processed from solution. *Science*, 310:462–465, 2005.
- [34] K. Gurumurugan, D. Mangalaraj, S.K. Narayandass, and C. Balasubramanian. Structural, optical and electrical properties of cadmium oxide films deposited by spray pyrolysis. *Phys. Stat. Sol. (a)*, 143(85):85–91, 1994.
- [35] R.B. Hall and H.H. Woodbury. The diffusion and solubility of phosphorus in cdte and cdse. *J. Appl. Phys.*, 39(12):5361–5365, 1968.
- [36] J.A. Hauch, P. Schilinsky, S.A. Choulis, R. Childers, M. Biele, and C.J. Brabec. Flexible organic p3ht:pcbm bulk-heterojunction modules with more than 1 year outdoor lifetime. *Sol. Energy Mater. Sol. Cells*, 92:727–731, 2008.
- [37] A.J. Heeger. Semiconducting and metallic polymers: the fourth generation of polymeric materials. *Synthetic Metals*, 125:23–42, 2002.

- [38] W.U. Huynh, J.J. Dittmer, W.C. Libby, G.L. Whiting, and A.P. Alivisatos. Controlling the morphology of nanocrystal-polymer composites for solar cells. *Adv. Funct. Mater.*, 13:73–79, 2003.
- [39] J. Jasieniak and P. Mulvaney. From cd-rich to se-rich-the manipulation of cdse nanocrystal surface stoichiometry. *J. Am. Chem. Soc.*, 129:2841–2848, 2007.
- [40] S. John, C. Soukoulis, M.H. Cohen, and E.N. Economou. Theory of electron band tails and the urbach optical-absorption edge. *Physical Review Letters*, 57(14):1777–1780, April 1986.
- [41] Z.H. Kafafi and P.A. Lane, editors. *Proceedings of SPIE Vol. 6334*, 2006.
- [42] G. Kalyuzhny and R.W. Murray. Ligand effects on optical properties of cdse nanocrystals. *J. Phys. Chem. B.*, 109:7012–7021, 2005.
- [43] J.Y. Kim, K. Lee, N.E. Coates, D. Moses, T.Q. Nguyen, M. Dante, and A.J. Heeger. Efficient tandem polymer solar cells fabricatd by all-solution processing. *Science*, 317:222–226, July 2007.
- [44] V. Komin, B. Tetali, V. Viswanathan, S. Yu, D.L. Morel, and C.S. Ferekides. The effect of cdcl₂ treatment on cdte/cds thin film solar cells studied using deep level transient spectroscopy. *Thin Solid Films*, 431-432:143–147, 2003.
- [45] G.H. Krause and E. Weis. The photosynthetic apparatus and chlorophyll fluorescence. an introduction. *Annu. Rev. Plant Physiol. Plant Mol. Biol.*, 42:313–349, 1991.
- [46] M. Kuno, J.K. Lee, B.O. Dabbousi, F.V. Mikulec, and M.G. Bawendi. The band edge luminescence of surface modified cdse nanocrystallites: Probing the luminescing state. *J. Chem. Phys.*, 106(23):9869–9881, 1997.
- [47] M. Kuno, J.K. Lee, B.O. Dabbousi, F.V. Mikulec, and M.G. Bawendi. The band edge luminescence of surface modified nanocrystallites: Probing the luminescing state. *J. Chem. Phys.*, 106:9869–9882, 1997.
- [48] Joseph R. Lakowicz. *Principles of Fluorescence Spectroscopy*. Springer Science+Business Media, 233 Spring Street, New York, NY 10013, USA, 2006. Third Edition.
- [49] S. Lalitha, R. Sathyamoorthy, S. Senthilarasu, and A. Subbarayan. Influence of cdcl₂ treatment on structural and optical properties of vacuum evaporated cdte thin films. *Sol. Energy Mater. Sol. Cells*, 90:694–703, 2006.
- [50] D.H. Levi, H.R. Moutinho, F.S. Hasoon, B.M. Keyes, R.K. Ahnrenkiel, M. Al-Jassim, L.L. Kazmerski, and R.W. Birkmire. Micro through nanostructure investigations of polycrystalline cdte: Correlations with processing and electronic structures. *Sol. Energy Mater. Sol. Cells*, 41/42:381–393, 1996.

- [51] G. Li, V. Shrotriya, Y. Yao, and Y. Yang. Investigation of annealing effects and film thickness dependence of polymer solar cells based on poly(3-hexylthiophene). *J. Appl. Phys.*, 98:043704, 2005.
- [52] L. L'uer, H.J. Egelhaaf, D. Oelkrug, G. Cerullo, G. Lanzani, B.H. Huisman, and D. de Leeuw. Oxygen-induced quenching of photoexcited states in polythiophene films. *Organic Electronics*, 5:83–89, 2004.
- [53] J.M. Luther, M. Law, M.C. Beard, Q. Song, M.O. Reese, R.J. Ellingson, and A.J. Nozik. Schottky solar cells based on colloidal nanocrystal films. *Nano Lett.*, 8(10):3488–3492, 2008.
- [54] Douglas Magde, Roger Wong, and Paul G. Seybold. *Fluorescence Quantum Yields and Their Relation to Lifetimes of Rhodamine 6G and Fluorescein in Nine Solvents: Improved Absolute Standards for Quantum Yields*, volume 54 of *Transactions of the Faraday Society*. 1958.
- [55] D.E. Markov, E. Amsterdam, P.W.M. Blom, A.B. Sieval, and J.C. Hummelen. Accurate measurement of exciton diffusion length in a conjugated polymer using a heterostructure with a side-chain cross-linked fullerene layer. *J. Phys. Chem. A*, 109:5266–5274, April 2005.
- [56] B.A. Mattis, P.C. Chang, and V. Subramanian. Effect of thermal cycling on performance of poly(3-hexylthiophene) transistors. *Mat. Res. Soc. Symp. Proc.*, 771:L10.35., 2003.
- [57] B.E. McCandless, H. Hichri, G. Hanket, and R.W. Birkmire. Vapor phase treatment of cdte/cds thin films with cdcl₂:0₂. In *Conf. Rec. 25th PVSC*, pages 781–784. IEEE, 1996.
- [58] B.E. McCandless, L.V. Moulton, and R.W. Birkmire. Recrystallization and sulfur diffusion in cdcl₂-treated cdte/cds thin films. *Prog. Photovoltaics Res. Appl.*, 5:249–260, 1997.
- [59] H.R. Moutinho, M.M. Al-Jassim, D.H. Levi, P.C. Dippo, and L.L. Kazmerski. Effects of cdcl₂ treatment on the recrystallization and electro-optical properties of cdte thin films. *J. Vac. Sci. Technol. A*, 16(3):1251–1257, 1998.
- [60] R.S. Muller and T.I. Kamins. *Device Electronics for Integrated Circuits*, pages 168–171. John Wiley & Sons, 1977.
- [61] A. Niemegeers and M. Burgelman. Effects of the au/cdte back contact on iv and cv characteristics of au/cdte/cds/tco solar cells. *J. Appl. Phys.*, 81(6):2881–2886, 1997.
- [62] A. Niemegeers and M. Burgelman. Effects of the au/cdte back contact on iv and cv characteristics of au/cdte/cds/tco solar cells. *J. Appl. Phys.*, 81(6):2881–2886, 1997.

- [63] D.W. Niles, D. Waters, and D. Rose. Chemical reactivity of cdcl_2 wet-deposited on cdte films studied by x-ray photoelectron spectroscopy. *Appl. Surf. Sci.*, 136:221–229, 1998.
- [64] D.I.K. Petritsch. *Organic solar cell architectures*. University of Cambridge, United Kingdom, July 2000.
- [65] C. Querner, P. Reiss, S. Sadki, M. Zagorska, and A. Pron. Size and ligand effects on the electrochemical and spectroelectrochemical responses of cdse nanocrystals. *Phys. Chem. Chem. Phys.*, 7:3204–3209, 2005.
- [66] I. Repins, M. Contreras, M. Romero, Y. Yan, W. Metzger, J. Li, S. Johnston, B. Egaas, C. DeHart, J. Scharf, B.E. McCandless, and R. Noufi. Characterization of 19.9%-efficient cigs absorbers. In *33rd IEEE Photovoltaic Specialists Conference*. IEEE, 2008.
- [67] M. Reyes-Reyes, K. Kim, and D.L. Carroll. High-efficiency photovoltaic devices based on annealed poly(3-hexylthiophene) and 1-(3-methoxycarbonyl)-propyl-1-phenyl(6,6) c_{61} blends. *Appl. Phys. Lett.*, 87:083506, 2005.
- [68] M. Jørgenson, K. Norrman, and F.C. Krebs. Stability/degradation of polymer solar cells. *Sol. Energy Mater. Sol. Cells*, 92:686–714, 2008.
- [69] E.H. Rhoderick and R.H. Williams. *Metal–Semiconductor Contacts*. Clarendon Press, 1988.
- [70] B.A. Ridley, B. Nivi, and J.M. Jacobson. All-inorganic field effect transistors fabricated by printing. *Science*, 286:746–750, 1999.
- [71] S.A. Ringel, A.W. Smith, M.H. MacDougal, and A. Rohatgi. The effects of cdcl_2 on the electronic properties of molecular-beam epitaxially grown cdte/cde heterojunction solar cells. *J. Appl. Phys.*, 70(2):881–889, 1991.
- [72] M. Saba, C. Ciuti, J. Bloch, V. Thierry-Mieg, R. André, Le Si Dang, S. Kundermann, A. Mura, G. Bongiovanni, J.L. Staehli, and B. Deveaud. High-temperature ultrafast polariton parametric amplification in semiconductor microcavities. *Nature*, 414:731–735, December 2001.
- [73] B.R. Saunders and M.L. Turner. Nanoparticle-polymer photovoltaic cells. *Adv. Colloid Interface Sci.*, 138:1–23, 2008.
- [74] E. Schibli and A.G. Milnes. Effects of deep impurities on n^+p junction reverse-biased small-signal capacitance. *Solid-State Electron.*, 11:323–334, 1968.
- [75] T. Schulmeyer, J. Fritsche, A. Thißen, A. Klein, W. Jaegermann, M. Campo, and J. Beier. Effect of in situ uhv cdcl_2 -activation on the electronic properties of cdte thin film solar cells. *Thin Solid Films*, 431-432:84–89, 2003.

- [76] A. Shah, P. Torres, R. Tscharnner, N. Wyrsh, and H. Keppner. Photovoltaic technology: the case for thin-film solar cells. *Science*, 285:692–698, July 1999.
- [77] W. Shockley and H.J. Queisser. Detailed balance limit of efficiency of p–n junction solar cells. *Journal of Applied Physics*, 32(3):6689–6692, March 1960.
- [78] V. Sholin, J.D. Olson, and S.A. Carter. Semiconducting polymers and quantum dots in luminescent solar concentrators for energy harvesting. *Journal of Applied Physics*, 101:1231114, June 2007.
- [79] G. Simons and J. McCabe. California solar resources. Technical Report CEC-500-2005-072-D, California Energy Commission, Sacramento, California, September 2005.
- [80] H. Sirringhaus, P.J. Brown, R.H. Friend, M.M. Nielsen, K. Bechgaard, B.M.W. Langeveld-Voss, A.J.H. Spiering, R.A.J. Janssen, E.W. Meljer, P. Herwig, and D.M. deLeeuw. Two-dimensional charge transport in self-organized, high-mobility conjugate polymers. *Nature*, 401:685–688, October 1999.
- [81] R. Stevenson. First solar: Quest for the \$1 watt. pages 26–32, August 2008.
- [82] A.J. Strauss. The physical properties of cadmium telluride. *Rev. Phys. Appl.*, 12:167–184, 1977.
- [83] B. Sun and N.C. Greenham. Improved efficiency of photovoltaics based on cdse nanorods and poly(3-hexylthiophene) nanofibers. *Phys. Chem. Chem. Phys.*, 8:3557–3560, 2006.
- [84] B. Sun, E. Marx, and N.C. Greenham. Photovoltaic devices using blends of branched cdse nanoparticles and conjugated polymers. *Nano Lett.*, 3:961–963, 2003.
- [85] B. Sun, H.J. Snaith, A.S. Dhoot, S. Westenhoff, and N.C. Greenham. Vertically segregated hybrid blends for photovoltaic devices with improved efficiency. *J. Appl. Phys.*, 97:014914, 2005.
- [86] S.M. Sze and K.K. Ng. *Physics of Semiconductor Devices*, pages 12–14,98,179. Wiley-Interscience, 2006.
- [87] J. Taylor, T. Kippeny, and S.J. Rosenthal. Surface stoichiometry of cdse nanocrystals determined by rutherford backscattering spectroscopy. *EJournal of Cluster Science*, 12(4):571–582, December 2001.
- [88] B.C. Thompson and J.M.J. Fréchet. Polymer-fullerene composite solar cells. *Angew. Chem. Int. Ed.*, 47:58–77, 2008.
- [89] B.C. Thompson and J.M.J. Fréchet. Polymer-fullerene composite solar cells. *Angew. Chem. Int. Ed.*, 47:58–77, 2008.

- [90] J. Toušek, D. Kindl, J. Toušková, and S. Dolhov. Diffusion length in cdte by measurement of photovoltage spectra in cds/cdte solar cells. *J. Appl. Phys.*, 89(1):460–465, 2001.
- [91] I. Turkevych, R. Grill, J. Franc, E. Belas, P. Höschl, and P. Moravec. High-temperature electron and hole mobility in cdte. *Semicond. Sci. Technol.*, 17:1064–1066, 2002.
- [92] A.K. Viswanath, J.I. Lee, D. Kim, C.R. Lee, and J.Y. Leem. Exciton-phonon interactions, exciton binding energy, and their importance in the realization of room-temperature semiconductor lasers based on gan. *Phys. Rev. B.*, 58(24):16333–16339, December 1998.
- [93] M. Wang, J.K. Oh, T.E. Dykstra, X. Lou, G.D. Scholes, and M.A. Winnik. Surface modification of cdse and cdse/zns semiconductor nanocrystals with poly(n,n-dimethylaminoethyl methacrylate). *Macromolecules*, 39:3664–3672, 2006.
- [94] G. Weber and F.W.J. Teale. Fluorescence excitation spectrum of organic compounds in solution. *Photochemistry and Photobiology*, 75(4):327–334, January 2002.
- [95] S.H. Wei and S.B. Zhang. Chemical trends of defect formation and doping limit in ii-vi semiconductors: The case of cdte. *Phys. Rev. B*, 66:155211, 2002.
- [96] J.H. Werner. Schottky barrier and pn-junction i/v plots—small signal evaluation. *Appl. Phys. A.*, 47:291–300, July 1998.
- [97] X. Wu. High-efficiency polycrystalline cdte thin-film solar cells. *Sol. Energy*, 77:803–814, 2004.
- [98] www.eia.doe.gov/cneaf/electricity/st_profiles/california.html, accessed 05/23/09, california electricity profile. Technical Report DOE/EIA-0348(01)/2, Energy Information Administration, Washington D.C., 2007.
- [99] K. Yang, Y. Wang, A. Jain, L. Samulson, and J. Kumar. Determination of electron and hole mobility of regioregular poly(3-hexylthiophene) by the time of flight method. *Journal of Macromolecular Science, Part A: Pure and Applied Chemistry*, 44:1261–1264, 2007.
- [100] S.B. Zhang, S.H. Wei, and A. Zunger. Phenomenological model for systematization and prediction of doping limits in $ii - -vi$ and $i - -iii - -vi_2$ compounds. *Journal of Applied Physics*, 83(6):3192–3196, March 1998.
- [101] U. Zhokhavets, T. Erb, H. Hoppe, G. Gobsch, and N.S. Sariciftci. Effect of annealing of poly(3-hexylthiophene)/fullerene bulk heterojunction composites on structural and optical properties. *Thin Solid Films*, 496:679–682, January 2006.

- [102] M. Zhu, T. Cui, and K. Varahramyan. Experimental and theoretical investigation of meh-ppv based schottky diodes. *Microelectronic Engineering*, 75:269–274, 2004.
- [103] K. Zweibel. Thin film pv manufactureing: Materials costs and their optimization. *Sol. Energy Mater. Sol. Cells*, 63:375–386, 2000.